Key Points:
- Sulfur isotopic compositions of sulfides in high-pressure rocks largely reflect their protolith compositions
- Slab fluids inherit the sulfur isotopic composition of their source
- Metasomatic sulfides exhibit a ~36 ‰ range in $\delta^{34}S$, which is consistent with large sulfate-sulfide fractionations during fluid migration

Isotopic Compositions of Sulfides in Exhumed High-Pressure Terranes: Implications for Sulfur Cycling in Subduction Zones

Jesse B. Walters[1] (iD), Alicia M. Cruz-Uribe[1], and Horst R. Marschall[2,3] (iD)

[1]School of Earth and Climate Sciences, Bryand Global Sciences Center, University of Maine, Orono, ME, USA, [2]Institut für Geowissenschaften, Geothe-Universität Frankfurt, Frankfurt, Germany, [3]Department of Geology and Geophysics, Woods Hole Oceanographic Institution, Woods Hole, MA, USA

Abstract Subduction is a key component of Earth's long-term sulfur cycle; however, the mechanisms that drive sulfur from subducting slabs remain elusive. Isotopes are a sensitive indicator of the speciation of sulfur in fluids, sulfide dissolution-precipitation reactions, and inferring fluid sources. To investigate these processes, we report $\delta^{34}S$ values determined by secondary ion mass spectroscopy in sulfides from a global suite of exhumed high-pressure rocks. Sulfides are classified into two petrogenetic groups: (1) metamorphic, which represent closed-system (re)crystallization from protolith-inherited sulfur, and (2) metasomatic, which formed during open system processes, such as an influx of oxidized sulfur. The $\delta^{34}S$ values for metamorphic sulfides tend to reflect their precursor compositions: −4.3 ‰ to +13.5 ‰ for metabasic rocks, and −32.4 ‰ to −11.0 ‰ for metasediments. Metasomatic sulfides exhibit a range of $\delta^{34}S$ from −21.7 ‰ to +13.9 ‰. We suggest that sluggish sulfur self-diffusion prevents isotopic fractionation during sulfide breakdown and that slab fluids inherit the isotopic composition of their source. We estimate a composition of −11 ‰ to +8 ‰ for slab fluids, a significantly smaller range than observed for metasomatic sulfides. Large fractionations during metasomatic sulfide precipitation from sulfate-bearing fluids, and an evolving fluid composition during reactive transport may account for the entire ~36 ‰ range of metasomatic sulfide compositions. Thus, we suggest that sulfates are likely the dominant sulfur species in slab-derived fluids.

Plain Language Summary Sulfur is one of the key ingredients for life and drives many biochemical and geochemical reactions in Earth systems. The exchange of sulfur between Earth's exterior and interior during subduction is an important long-term component of the global sulfur cycle. In our study, we use stable isotopes of sulfur as a tracer of sulfur loss and migration from subducting oceanic plates. We demonstrate the utility of sulfur isotopes as a tracer by identifying potential sources of sulfur in the subducting plate. We suggest that the isotopic composition is unaffected by the dissolution of sulfur-bearing minerals and infer that the large compositional range of sulfides formed from fluids expelled from the subducting plate reflect the speciation of sulfur in the fluid. This study represents the first global overview of sulfur isotopes in subducted metamorphic rocks. These data may be compared with sulfur isotope measurements in volcanic arcs overlying subduction zones to trace sulfur from the subducting plate through the overriding plate.

1. Introduction

Subduction is the primary mechanism of mass transfer between the surface and deep Earth and plays a critical role in the cycling of many major, minor, and trace elements on geologic time scales (e.g., Hermann et al., 2006; Schmidt & Poli, 2003; Spandler & Pirard, 2013). The transfer of elements between the subducting slab, slab-mantle interface zone, and into the overlying magmatic arc system is controlled, in part, by the ability of elements to be liberated as soluble species during slab devolatilization. Increasing pressure and temperature conditions during subduction drive metamorphic reactions in the slab to produce hydrous fluids or silicate melts, which transport material into the overlying system that eventually produces the magmatic arc (e.g., Hacker, 2008; Manning, 2004; Marschall & Schumacher, 2012). Despite the important role sulfur may play in the redox of the slab-arc system and trace metal cycling, a limited number of studies have focused on sulfur mobilization from the slab during subduction metamorphism (Alt, Shanks, et al., 2012, Alt, Garrido, et al., 2012; Canil & Fellows, 2017; Crossley et al., 2018; Debret & Sverjensky, 2017; Evans &

Powell, 2015; Evans et al., 2014, 2017; Jego & Dasgupta, 2013; LaFlamme et al., 2018; Lee et al., 2018; Tomkins & Evans, 2015).

Sulfur is one of the six most abundant elements in the Earth (~2 wt %) and is subducted at a rate of 2.31–2.83 $\times 10^{12}$ mol/year (Dreibus & Palme, 1996; Evans, 2012). Like carbon, sulfur is one of the few elements to naturally exhibit a wide range of valence states (S^{2-} to S^{6+}). One mole of sulfur has the potential to oxidize or reduce up to eight moles of iron; therefore, even small additions of subducted sulfur to the mantle may have wide-ranging implications for mantle fO_2 through geologic time. Additionally, dissolved sulfur acts as a complexing ligand with some metals and is a required coprecipitant to draw other metals out of solution (e.g., Pokrovski et al., 2008, 2015; Seo et al., 2009; Zajacz et al., 2011). The release of various sulfur species from different slab depths has been postulated to explain the distribution of arc-related ore deposits (Pokrovski et al., 2015; Tomkins & Evans, 2015). Thus, quantifying the amount of sulfur liberated during subduction, the migration of sulfur from the slab into the volcanic arc and the oxidation state of sulfur leaving the slab are critical to all studies of arc-related ore deposits, and magma and mantle geochemistry.

Sulfur isotope ratios of $^{34}S/^{32}S$, expressed as $\delta^{34}S$ in per mil relative to the meteorite standard Vienna Canyon Diablo Troilite, are commonly used as an isotopic tracer in a variety of geologic and biologic systems. Mass-dependent sulfur isotope fractionation is influenced by temperature, fO_2-fS_2, and pH, and may occur during chemical exchange between sulfur species or anaerobic respiration by sulfur-reducing bacteria (see reviews in Canfield, 2004; Seal, 2006). Combined with mass-independent sulfur fractionations in the early Earth, these processes have introduced significant isotopic heterogeneity to surface and mantle reservoirs (Figure 1). Early studies of mid-ocean ridge basalts (MORBs) reported $\delta^{34}S$ values indistinguishable from the chondritic average of +0.04 $\pm$ 0.31 ‰ (Gao & Thiemens, 1993a, 1993b; Sakai et al., 1984; Thode et al., 1961). Recent studies of MORB by Labidi et al. (2012, 2013, 2014) identify $\delta^{34}S$ values of −1.9 ‰ to +0.6 ‰ with a dominance of analyses <0 ‰. Correlation of $\delta^{34}S$ values with $^{87}Sr/^{86}Sr$ and $^{143}Nd/^{144}Nd$ identify a depleted mantle reservoir with an average of −1.28 $\pm$ 0.66 ‰, highlighting a distinct depletion in $^{34}S/^{32}S$ relative to chondrites (Labidi et al., 2013). Further highlighting mantle heterogeneity, whole rock and sulfide compositions for subcontinental lithospheric xenoliths range from −6 ‰ to +11 ‰ (Chaussidon et al., 1989; Chaussidon & Lorand, 1990; Giuliani et al., 2016; Ionov et al., 1992; Kyser, 1990; Tsai et al., 1979; Wilson et al., 1996). Sulfide inclusions in eclogitic diamonds display a wide range of $\delta^{34}S$ values from −11 ‰ to +14 ‰, whereas inclusions in peridotitic diamonds have a more restricted range of −5 ‰ to +6 ‰ (Cartigny et al., 2009; Chaussidon et al., 1987; Eldridge et al., 1991, 1995; Farquhar et al., 2002; Rudnick et al., 1993; Thomassot et al., 2009). Recent studies of ocean island basalts highlight excursions in $\delta^{34}S$ values to nearly −18 ‰ (Cabral et al., 2013; Delevault et al., 2016). The recycling of sulfur during subduction has long been invoked to account for some of these variations (e.g., Chaussidon et al., 1989; Eldridge et al., 1991; Farquhar et al., 2002; Giuliani et al., 2016; Labidi et al., 2013).

The sulfur isotopic composition of surface reservoirs has deviated greatly from the bulk Earth. Sulfate dissolved in seawater is the largest surface reservoir of sulfur, and modern seawater has a $\delta^{34}S$ value of +21.0 $\pm$ 0.2 ‰ (Figure 1; Rees et al., 1978). Although rare in the absence of large evaporite basins, chemical precipitation of seawater sulfate results in only minor fractionation between dissolved sulfate and the sulfate precipitate. Conversely, fractionation during bacterial sulfate reduction at the seafloor produces a range in $\delta^{34}S$ values of −50 ‰ to +20 ‰ in seafloor sedimentary pyrite (Figure 1), though ~87 % of all analyses are less than −10 ‰ (Canfield & Farquhar, 2009). Bacterial sulfate reduction during off-axis hydrothermal alteration can produce local $\delta^{34}S$ variations of −72 ‰ to +17 ‰ in the altered oceanic crust (AOC; Alford et al., 2011; Alt, 1995; Alt & Shanks, 2011; Lever et al., 2013; Ono et al., 2012; Rouxel et al., 2008). Here we use AOC to refer to the altered mafic crust, including the upper volcanics, sheeted dikes, and gabbros. Sulfur isotope mass-balance constraints for deeply cored sections of AOC from Ocean Drilling Program/International Ocean Discovery Program holes 504B and 1256D give overall isotopic compositions of +0.9 ‰ and −6 ‰, respectively (Alt, 1995; Alt & Shanks, 2011). Both abiotic and biotic fractionations also occur during serpentinization of the lithospheric mantle; serpentinites formed at high temperatures typically have $\delta^{34}S$ values of +5 ‰ to +10 ‰, whereas $\delta^{34}S$ values of −45 ‰ to +27 ‰ have been reported for low-temperature serpentinites (Figure 1; see review in Alt et al., 2013). Sulfur isotope analyses of arc volcanic products show variability in $\delta^{34}S$ values of up to 26 ‰ (Figure 1; Alt et al., 1993; de Hoog et al., 2001; Mandeville et al., 1998, 2009; Marini et al., 1994, 1998; Robinson & Graham, 1992; Rye et al., 1984; Ueda & Sakai, 1984; Woodhead
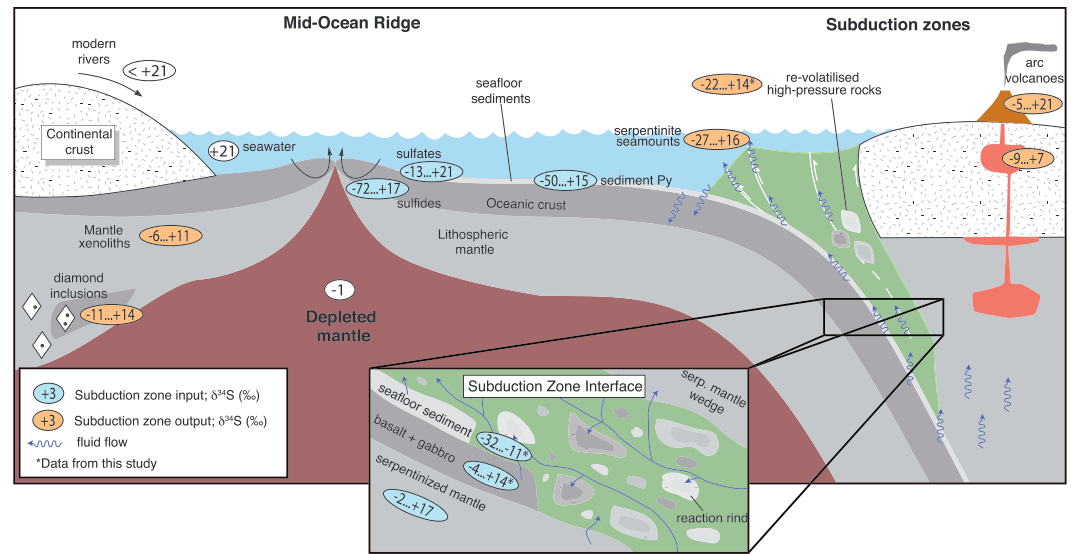
Figure 1. Schematic cross section through the crust and uppermost mantle presenting the exchange of sulfur between surface and mantle reservoirs. The isotopic values for sulfur inputs (green) and outputs (orange) are displayed. The inset illustrates erosion of the slab-mantle interface and mélange anatomy. Fluids leaving the slab are expected to mix along the subduction zone interface and flux the overlying mantle wedge to initiate melting. Isotopic compositions for subducted and exhumed rocks are from this study, Bebout (1995), Crossley et al. (2018), Evans et al. (2014), Giacometti et al. (2014), and Shimizu et al. (2013). The range of altered oceanic crust values are from Alford et al. (2011), Alt (1995), Alt & Shanks (2011), Ono et al. (2012), and Rouxel et al. (2008). The values for seawater sulfate and sedimentary pyrite are from Rees et al. (1978) and Canfield & Farquhar (2009), respectively. The upper limit for modern riverine sulfate is given in the review of Bottrell & Newton (2006). The value for depleted mantle is from Labidi et al. (2013, 2014). The range for sulfide inclusions in diamond are from Cartigny et al. (2009), Chaussidon et al. (1987), Eldridge et al. (1991, 1995), Farquhar et al. (2002), Rudnick et al. (1993), and Thomassot et al. (2009). Subcontinental mantle xenolith values are from Chaussidon & Lorand (1990), Chaussidon et al. (1989), Giuliani et al. (2016), Ionov et al. (1992), Kyser (1990), Tsai et al. (1979), and Wilson et al. (1996). Serpentinite seamount values come from Alt & Shanks (2006) and Aoyama et al. (2018). Whole rock data for arc volcanic products include those from Alt et al. (1993), de Hoog et al. (2001), Mandeville et al. (1998, 2009), Marini et al. (1994, 1998), Robinson & Graham (1992), Rye et al. (1984), Ueda and Sakai (1984), and Woodhead et al. (1987). Volcanic arc melt inclusion data are from Bouvier et al. (2008).

et al., 1987). Magmatic processes, such as phase separation and degassing, as well as the influence of evolving fO_2, temperature, pressure, and alteration of volcanic products, are variably responsible for the 26 ‰ variation in $\delta^{34}S$ values, and significantly complicate the ability to isotopically fingerprint magmatic sulfur sources (see review in Marini et al., 2011). Melt inclusions may be less sensitive to degassing processes, but only a restricted set of data currently exist (Figure 1; Bouvier et al., 2008).

The difficulty of using sulfur isotope measurements on volcanic products as a means to investigate sulfur recycling during subduction highlights the need for the direct analyses of sulfur-bearing phases in high-pressure exhumed terranes. To date, $\delta^{34}S$ measurements from exhumed metamorphic terranes have been reported from primarily eclogite-facies rocks from only five localities worldwide (Bebout, 1995; Evans et al., 2014; Giacometti et al., 2014; Lee et al., 2018). In addition, sulfur isotope compositions for high-pressure serpentinites have been reported for only five localities (Alt, Shanks, et al., 2012, Alt, Garrido, et al., 2012; Crossley et al., 2018; Lee et al., 2018; Shimizu et al., 2013). However, questions remain regarding the ability for sulfides to retain their protolith-inherited isotopic composition during high-pressure metamorphism and mechanisms that drive sulfur loss from the slab.

In this study we employ *in situ* ion microprobe analyses to determine the sulfur isotope composition of sulfides from nine exhumed subduction zone terranes worldwide. We report $\delta^{34}S$ values of pyrite, pyrrhotite, and chalcopyrite in samples that span a range of pressure-temperature (*P-T*) conditions, compositions, and ages. The investigated sulfides include those formed at prograde and peak metamorphic conditions, as well as those formed due to metasomatism (i.e., jadeitite formation and rehydration during exhumation). Prograde and peak metamorphic sulfides may shed light on the isotopic composition of subduction zone

sulfur inputs, whereas sulfides in revolatilized high-pressure and hybrid rocks provide a means of examining the isotopic composition of slab-derived fluids. Utilizing this sample suite, we assess the mechanisms of sulfide petrogenesis, the effects of diffusion on sulfur isotope composition, and the sulfur isotope distribution across different generations of sulfides, lithologies, and geologic time. We apply this global data set to estimates of the isotopic composition and redox state of dissolved sulfur liberated from subducted slabs.

2. Sampling Strategy and Sulfide Petrography

2.1. Sampling Strategy

Unfortunately, no single exhumed terrane on Earth exhibits the full range of subduction zone pressure-temperature (*P-T*) conditions or lithologic variation. Instead, the exhumed rock record is incomplete, and the full picture can only be reconstructed by combining evidence from various global localities. In addition, late-stage alteration during exhumation, surficial weathering, and sulfur loss during subduction result in the variable preservation of sulfides. Therefore, we studied exhumed high-pressure rocks collected from nine localities that cover a wide set of conditions and have protolith ages ranging from the Proterozoic to the Paleogene. Sulfide-bearing samples were sourced from both coherent lithotectonic units (e.g., Czech Republic and Austria) and mélange zones (e.g., Dominican Republic and Greece) to span a large range of lithologies and peak metamorphic conditions. Samples are referred to in the text by their country (or state) of origin. Specific localities are listed in Table 1, and detailed geologic background and petrography can be found in supporting information Text S1. Petrographic and isotopic analyses of this sample set allow for a comparison through geologic time and highlight important similarities across a variety of tectonic environments. We recognize that variations in subduction zone thermal structure, subducted lithologies, and age complicate direct comparison across our sample suite; however, we show consistent trends across localities and provide a first-order examination of potential processes affecting sulfur in subducting slabs.

2.2. Sulfide Petrography

Sulfides are broadly classified as either metamorphic or metasomatic (Table 1 and Figure 2). Metamorphic sulfides are associated with prograde to peak textures, such as isolated inclusions in garnet, or on the basis of inclusion assemblages in matrix sulfides (Figures 2a–2c). Metamorphic sulfide inclusions of pyrite, pyrrhotite, chalcopyrite, and galena in garnet were observed in samples from the Czech Republic (SVS-11-01, TIS-11-2), France (GO83-12), Dominican Republic (DR1203-11-03), Greece (SY403), and California (K12). No prograde inclusions exhibit coexisting pyrite and pyrrhotite. Peak metamorphic pyrrhotite was not observed, whereas peak metamorphic matrix pyrite and chalcopyrite were observed in two samples from the Tauern Window in Austria (DT119) and Franciscan complex in California (K12). Pyrite grains in the graphitic schist sample DT119 are elongate parallel to the peak metamorphic foliation. Pyrite is also intergrown with honeycomb garnet (Figure 2b), which has been interpreted to form at peak conditions (Hawkins et al., 2007). These observations suggest pyrite stability at 1.66–2.05 GPa and 540–584 °C (Dachs & Proyer, 2001). Inclusions of spessartine within pyrite and growth of stilpnomelane (K $(Fe^{2+},Mg,Fe^{3+})_8(Si,Al)_{12}(O, OH)_{27}\cdot n(H_2O)$) around pyrite in quartzite sample K12 place pyrite formation at or near the metamorphic peak (Figure 2c). However, *P-T* conditions of this locality are poorly constrained (see discussion in Text S1).

The majority of sulfides in the sample suite are classified as metasomatic and are texturally associated with two broad types of metasomatism (Table 1): "blackwall" reaction zones between high-grade blocks and mélange-matrix, and retrograde rehydration during exhumation of large tectonic slices. Following the incorporation of crustal fragments into the slab-mantle interface, large chemical gradients, an abundance of fluids, and deformation lead to the progressive digestion of high-grade blocks to produce hybridized mixed compositions (see discussions in Bebout & Barton, 1989 and Marschall & Schumacher, 2012).

Sulfides in the serpentinite block-and-matrix mélange exposed on the island of Syros, Greece, are almost exclusively restricted to blackwall zones (Figure 3). On the microscale, inclusions of omphacite and rutile occur in pyrite in a garnet-omphacite-chlorite reaction rind (SY462), whereas pyrite is also observed in glaucophanite and chlorite schist rinds (SY404). These observations suggest that sulfide deposition occurred following block incorporation into the subduction interface at peak eclogite-facies conditions and continued through blueschist-facies retrogression. Similarly, sulfides from mélange in the Dominican Republic and Australia are also largely associated with zones of mixed compositions (Table 1), where blackwall minerals

Table 1
Summary of Sulfide Petrography

Locality, country of origin	Sample	Rock type	Alteration type	Metamorphic sulfides[a]	Metasomatic sulfides[a]
Světlík-Stís, CZ	SVS-11-1	Eclogite	Granulite- to amphibolite-facies	Po + Ccp in Grt	Vein Py w/incls of Di + Pl symplectite, rimmed by Po + Ccp + Ths
Tisova, CZ	TIS-11-2	Eclogite	Granulite- to ammphibolite-facies		Vein Py w/incls of Di + Pl symplectite, rimmed by Po + Ccp + Ths
Frosnitz V., AT	FT105B	Calc-schist	Greenscist-facies		Py + Ccp ± Bn w/retrograde Bt + Hbl + Ep + Mt after Grt
	DT119A	Calc-schist		Ccp in Grt w/Gr, lineated Py + Ccp	
P. Macquarie, AU	PMQ06-	Banded blueschist	Blackwall Zone		Py ± Ccp + Po in veins and overgrowing peak foliation
Vendée, FR	G083-12	Metagabbroic eclogite	Granulite- to ammphibolite-facies	Ccp + Py in Grt	Py ± Ccp + Tsp adjacent to Hbl + Chl and Di + Pl after Grt + Omp
Jagua Clara M., DR	DR1203-10-02	Blueschist	Greenscist-facies		Po + Ccp in veins of Pmp + Chl + Ep
	DR1203-11-03	Grt blueschist	Blueschist- to Greenschist-facies	Py + Ccp in Grt	Py + Ccp + Po in cracks in Grt w/Chl, Py w/retrograde Ab + Ttn
	DR1203-15-02	Chl schist	Blackwall Zone		Py w/incls of Ap + Ccp
	DR1203-07-02	Jadeitite	Blackwall Zone		Py w/incls of Ccp + Gn, rare matrix Ccp
Franciscan Complex, US	K12	Sps quartzite	Blackwall Zone	Py with Grt incls ± Ccp + Sph, Gn in Grt	
Syros, GR	SY404	Chl-Act schist	Blackwall Zone		Py w/incls of Chl + Ap
	SY328	Omp - Chl fels	Blackwall Zone		Py w/incls of Ccp + Bn
	SY403	Grt Blueschist		Py in Grt	
	SY462	Grt - Omp - Chl fels	Blackwall Zone		Py w/incls of Omp + Rt/Ilm + Ep/Aln ± Ab
	SY510	Metagabbroic eclogite		Py, Ccp in Omp	

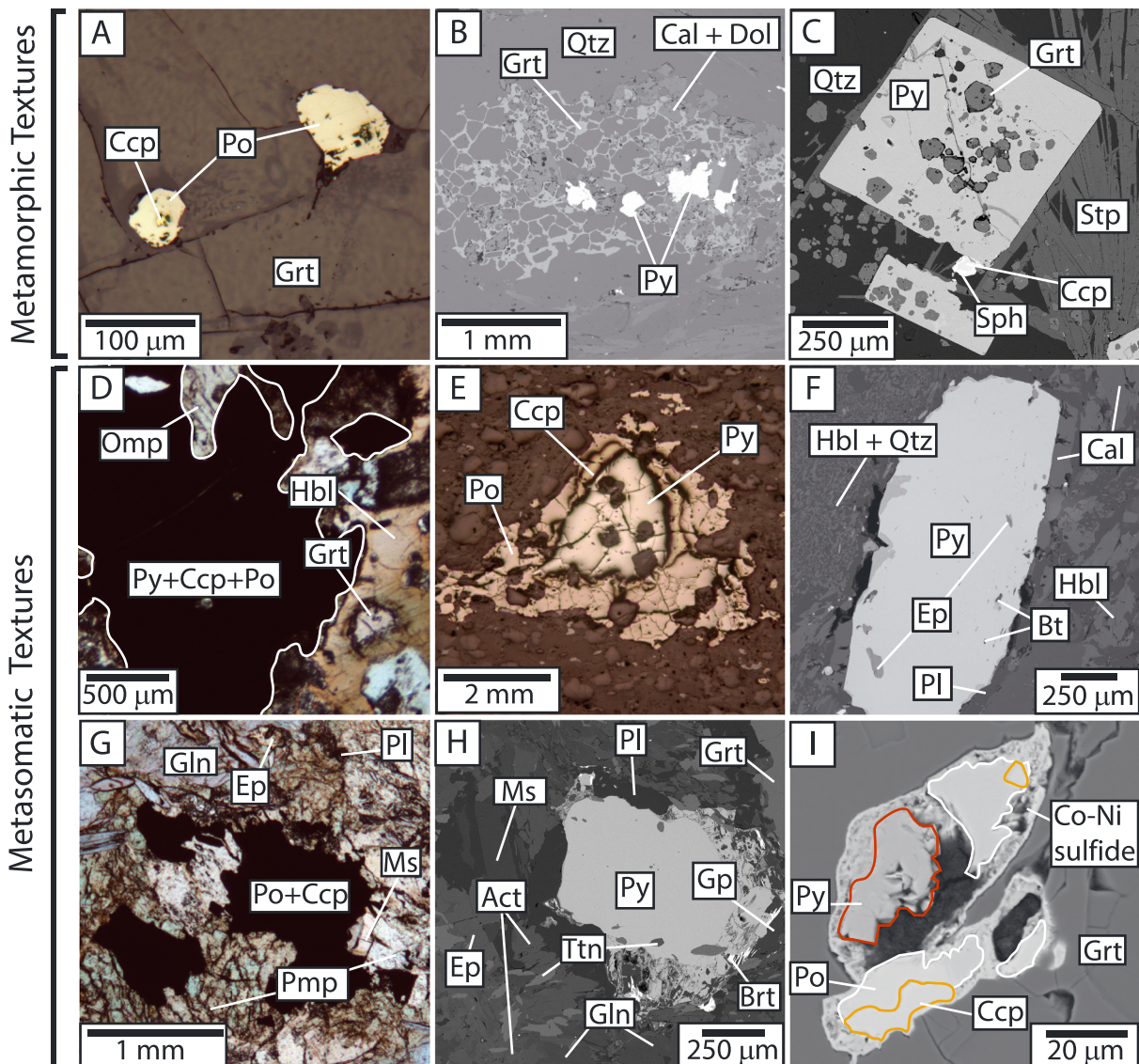[a]Abbreviations after Whitney and Evans (2010), except for thiospinel (Ths).

Figure 2. Transmitted light, reflected light, and backscattered electron images of key microtextures: (a) Prograde inclusions of Po + Ccp in garnet in sample SVS-11-01, (b) Py + Qz + Cal + Dol intergrown with honeycomb garnet in sample DT119, (c) Inclusions of garnet in pyrite with stilpnomelane and quartz in sample K12, (d) Hornblende exhibiting dark to light Fe/Mg zonation adjacent to a mass of Py + Ccp + Po (black) in sample SVS-11-01, (e) Pyrite overgrown by Ccp + Po in a vein of Di + Pl symplectite in sample TIS-11-02, (f) Bt + Ep inclusions in pyrite in sample FT105B, (g) Po + Ccp in a vein of Pmp + Chl + Ms in sample DR1203-10-02, (h) pyrite with inclusions of titanite adjacent to plagioclase in sample DR1203-11-03, and (i) crack filling Py (red) + Po (white) + Ccp (yellow) rimmed by Co-Ni sulfide in sample DR1203-11-03. Mineral abbreviations follow Whitney & Evans (2010).

occur as inclusions in sulfide and sulfides exhibit crosscutting relationships with the peak metamorphic foliation. Samples DR1203-10-02 and DR1203-11-03 were collected from riverwashed boulders and do not preserve intact core-rind-matrix relationships; however, their textures are consistent with blackwall metasomatism. Sulfides in sample 10-02 are restricted to veins of pumpellyite, chlorite, and white mica (Figure 2g), and the association of sulfides in sample 11-03 with chlorite, titanite, albite, and brittle fractures in garnet (Figures 2h and 2i) suggests a retrograde fluid-driven origin (Table 1).

Metasomatic sulfides that formed during rehydration in rocks exhumed within tectonic slices are associated with various stages of granulite-, amphibolite-, and greenschist-facies metamorphism. Sulfides in rocks exhumed through the granulite- and amphibolite-facies (SVS-11-01, TIS-11-02, and GO83-12) contain metasomatic sulfides that are associated with retrograde hornblende ± chlorite (e.g., Figure 2d). In two samples from the Czech Republic, masses of pyrite rimmed by chalcopyrite and pyrrhotite occur in veins of diopside +
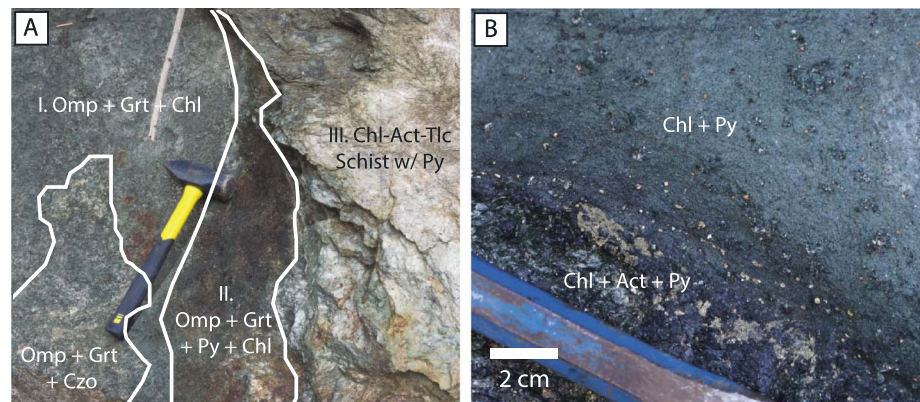
Figure 3. Field photographs from Syros, Greece, illustrating macroscale relationships between sulfide abundance and blackwall zones. Panel (a) highlights overprinting of the metagabbroic peak eclogite facies assemblage (omphacite + garnet + clinozoisite) by three successive blackwall zones: (I) omphacite-garnet-chlorite fels, (II) omphacite-garnet-chlorite fels with pyrite, and (III) pyrite-bearing chlorite-actinolite-talc schist. Panel (b) shows a pyrite-rich zone at the contact between chlorite schist and chlorite-actinolite schist in the outer metasomatic rinds of another block.

plagioclase symplectite after omphacite (Figures 3d and 2e; Faryad et al., 2006; O'Brien, 1997). Inclusions of diopside + plagioclase symplectite and retrograde hornblende are found within the central pyrite grains, suggesting that pyrite formed during or following the granulite-facies overprint. A compositional gradient of decreasing Fe/Mg in hornblende adjacent to pyrrhotite is consistent with pyrite breakdown to pyrrhotite, which requires approximately a twofold increase in Fe atoms per formula unit. Therefore, pyrite breakdown to pyrrhotite and chalcopyrite likely occurred during rehydration and amphibole formation. Pyrrhotite also contains inclusions of thiospinel, which are not found within pyrite and likely formed during pyrite breakdown.

Similarly, metasomatic sulfides in sample FT105B from the Frosnitz Valley in Austria contain inclusions of retrograde phases, such as epidote, and occur in domains of garnet and phengite retrogression to biotite, hornblende, epidote, and skeletal magnetite (e.g., Figure 2f). Evans et al. (2014) similarly observed sulfides associated with blueschist- and greenschist-facies retrogression in rocks from the Zermatt-Saas Zone (Switzerland) and from New Caledonia. Sulfides associated with granulite- to greenschist-facies retrogression demonstrate the fluid mobility of sulfur over a wide range of *P-T* conditions during the exhumation of large tectonic slices at convergent margins.

3. Analytical Methods

3.1. Trace Element Maps

Samples were prepared as 1-in. (2.54 cm) round polished sections or epoxy grain and rock mounts. Prior to isotopic analysis, trace element maps of Co, As, and Ni in pyrite were collected using a Cameca SX-100 electron probe microanalyzer housed at the University of Maine equipped with four wavelength-dispersive spectrometers. Trace element maps were used to target specific zones of sulfide grains for ion probe analysis to better constrain spatial and temporal sulfur isotopic variation. Operating conditions for qualitative Co, As, and Ni maps were 20 kV accelerating voltage, 100 nA beam current, and a dwell time of 30 ms. Exploratory maps of pyrrhotite and chalcopyrite revealed that Co, As, and Ni were below the detection limit or lacked zoning.

3.2. Secondary Ion Mass Spectrometry

Sulfur isotope analyses were conducted using secondary ion mass spectrometry with a Cameca IMS 1280 housed at the Northeast National Ion Microprobe Facility, Woods Hole Oceanographic Institution. Polished sections and mounts were coated with 100–125 nm of high-purity gold. A 1-nA $^{133}Cs^+$ beam was focused to ~10-μm diameter to collect background (at mass 31.7), ^{32}S, and ^{34}S using a Faraday cup detector in sequential mode. Sulfides exhibit high conductivity, negating the need for an electron gun. In all cases, a secondary ion accelerating voltage of 10 kV, energy window of 60 V without offset, and a mass resolving power of 4,000 were used. The mass resolving power was calculated as the mass/Δmass at 10 % peak height. All data are reported as $\delta^{34}S$ (‰) relative to Vienna Canyon Diablo Troilite standard (Tables 2 and S1–S6).

Table 2
Summary of 2016–2017 Sulfur Isotope Analyses ($\delta^{34}S$, ‰)

Locality	Sample	Phase	Type	Min	Max	Ave.	2SE[a]
Světlik-Sŭs	A. SVS-11-1	Py ($n = 3$)	Metasomatic	−3.3	-1.5	-2.5	1.1
		Po ($n = 3$)	Metasomatic	−2.5	-2.0	-2.4	0.4
		Po ($n = 7$)	Metamorphic	−4.3	-1.7	-2.9	0.9
		Ccp ($n = 3$)	Metasomatic	−2.2	-1.2	-1.8	0.6
Tisova	B. TIS-11-2	Py ($n = 5$)	Metasomatic	3.7	7.8	5.2	1.5
		Po ($n = 3$)	Metasomatic	3.3	4.2	3.9	0.6
		Ccp ($n = 2$)	Metasomatic	3.9	0.8	4.6	1.5
Frosnitz V.	C. FT105B	Py ($n = 17$)	Metasomatic	8.4	13.9	11.1	0.8
		Ccp ($n = 3$)	Metasomatic	6.2	10.8	8.1	2.8
	D. DT119A	Py ($n = 10$)	Metamorphic	−26.8	−22.0	−25.2	1.0
		Ccp ($n = 1$)	Metamorphic			−31.1	
P. Macquarie	E. PMQ06-5	Py ($n = 8$)	Metasomatic	−9.0	−7.3	−8.0	0.4
		Ccp ($n = 3$)	Metasomatic	−9.0	−5.4	−6.7	2.4
Vendée	F. G083-12-3	Py ($n = 5$)	Metasomatic	4.0	5.2	4.6	0.4
		Py ($n = 4$)	Metamorphic	0.7	6.7	2.5	2.8
		Ccp ($n = 2$)	Metasomatic	4.1	4.5	4.3	0.5
		Ccp ($n = 1$)	Metamorphic			4.3	
Jagua Clara M.	G. DR1203-10-02	Po ($n = 4$)	Metasomatic	−20.9	−19.3	−20.7	1.0
		Ccp ($n = 2$)	Metasomatic	−20.6	−20.7	−20.6	0.1
	H. DR1203-11-03	Py ($n = 3$)	Metasomatic	−1.7	−0.4	−1.2	0.8
		Po ($n = 4$)	Metasomatic	−5.5	−3.2	−4.0	1.1
		Po ($n = 1$)	Metamorphic			2.2	
		Ccp ($n = 1$)	Metasomatic			−3.2	
	I. DR1203-15-02	Py ($n = 3$)	Metasomatic	−3.8	−2.2	−2.8	1.1
	J. DR1203-07-02	Py ($n = 11$)	Metasomatic	−2.2	12.5	3.9	3.3
		Ccp ($n = 2$)	Metasomatic			3.1	1.3
Laytonville Q.	K. K12	Py ($n = 13$)	Metamorphic	−30.9	−11.0	−24.3	4.8
		Ccp ($n = 3$)	Metamorphic	−14.7	−12.4	−13.3	1.4
Syros	L. SY404	Py ($n = 7$)	Metasomatic	−4.5	−0.9	−2.2	1.0
	M. SY328	Py ($n = 4$)	Metasomatic	−8.0	−6.7	−7.4	0.5
	N. SY523	Py ($n = 4$)	Metasomatic	2.1	4.7	3.4	1.1
	O. SY462	Py ($n = 8$)	Metasomatic	−1.3	7.3	3.3	1.7

[a]Standard error of the mean for n analyses.

For pre-2016 analyses, a $30 \times 30\ \mu m^2$ raster was used and spots were presputtered for 240 s. Background, ^{32}S, and ^{34}S were collected for 2, 5.04, and 15.04 s, respectively. A settling time of 3.04 s was applied to each mass. A background of ~50×10^4 cps was measured on mass 31.7, which corresponds to ~0.05 % and ~1 % of the count rates for ^{32}S and ^{34}S, respectively. The total analysis time was ~30 min for a total of 50 cycles.

An improved analytical protocol was used for 2016–2017 sessions. For these analyses, trace element maps were used to select locations for SIMS analyses. Spots were presputtered for 180 s, and analyses were made using a $20 \times 20\ \mu m^2$ raster. Masses of ^{32}S and ^{34}S were counted for 2.00 and 5.04 s, respectively, with a 2.5 s settling time on each. The background was negligible (~200 cps) and not measured during analyses. The total analysis time was ~7 min for a total of 19 cycles.

Short- and long-term variations in the instrumental mass fractionation were monitored using at least five reference analyses collected before and after each session, with additional reference analyses between every 10 or fewer unknown analyses. For pre-2016 sessions, long analysis times precluded more frequent reference analyses and only one to three analyses were conducted immediately before and after each group of ≤10 unknowns. The following international sulfur isotope reference materials were used to correct for instrumental mass fractionation: Balmat pyrite (+15.1 ± 0.2 ‰; Crowe & Vaughan, 1996), MVE pyrite (−13.2 ‰), Ruttan pyrite (+1.2 ± 0.1 ‰; Crowe & Vaughan, 1996), Norilsk chalcopyrite (+8.0 ± 0.2 ‰; Crowe & Vaughan, 1996), Trout Lake chalcopyrite (+0.3 ±0.2 ‰; Crowe & Vaughan, 1996), M8534 pyrrhotite (+3.6 ‰), and 31560 pyrrhotite (+7.4 ‰). All data are tabulated in Tables S1–S6, with reference material analyses given in Tables S7–S23. Uncertainties (2SE) include random analytical uncertainties, which propagate to 0.1–1.5 ‰ and 0.1–0.5 ‰ for pre-2016 and 2016–2017 sessions, respectively. The reproducibility of

reference materials (2σ systematic uncertainties) was calculated for each analytical session and ranges from 0.6–3.5 ‰ and 0.5–1.8 ‰ for pre-2016 and 2016–2017 sessions, respectively.

4. Results

Trace element maps and sulfur isotope data are summarized below and refer to 2016–2017 data, except where noted. Sulfur isotope analyses performed during 2016–2017 are summarized in Table 2, and all data are included in Figure 4. Full results, including pre-2016 analyses, are tabulated in Tables S1–S6 and are discussed on a sample-by-sample basis in supporting information Text S2. For textural context all 2016–2017 sulfur isotope analyses are plotted on photomicrographs, backscattered electron images, and trace element maps in Figures S1–S15.

4.1. Mafic Samples

Eight inclusions of metamorphic sulfides in garnet were found to exhibit a range from –4.3 ‰ to +14.1 ‰, with 77 % of δ^{34}S values ($n = 13$) between −5 ‰ and +5 ‰ (Figure 4). Three pyrite inclusions in garnet with δ^{34}S values higher than +5 ‰ were identified in a garnet blueschist from Syros (sample SY403). Although systematic uncertainties are high for these analyses ($2\sigma_{sys} = 3.5$ ‰), δ^{34}S values at +10.9 ‰ and +14.1 ‰ are statistically different from +5 ‰. Metamorphic sulfide inclusions in garnet from samples with mid-Paleozoic (sample SVS-11-01, Czech Republic) and Precambrian (sample G083-12, France) protoliths display a range from −4.3 ‰ to +6.7 ‰ (Figure 5C&F). Additionally, multiple spots on a pyrite grain in sample G083-12 reveal +6.7 ‰ to +0.7 ‰ core to rim variation (Figure 5F).

In contrast, metasomatic sulfides in mafic rocks exhibit a much larger ~29 ‰ range from −20.9 to +13.5 ‰ (Figure 4). Matrix sulfides in a metagabbroic eclogite from Syros, Greece (SY510), display large intergrain variability, with a range of +1.3 ‰ to +13.5 ‰. Single sulfide grains exhibit up to ~4 ‰ variation in $\delta34$S values, which are variably coupled with trace element zoning patterns. For example, pyrite in samples from two localities in the Czech Republic (SVS-11-01, Figures 5a and 5b, and TIS-11-02, Figure 6a) display low-Co cores and high-Co rims; however, δ^{34}S values in SVS-11-01 display a core to rim increase from −2.7 ‰ to −1.5 ‰, whereas δ^{34}S values in TIS-11-02 display a core to rim decrease from +7.9 ‰ to +4.7 ‰. Additionally, isotopic variation of 0.7 ‰ to 1.4 ‰ is observed within single zones.

4.2. Sedimentary Samples

Analyses of metamorphic sulfides in two metasedimentary samples from California (K12) and Austria (DT119A) display ranges from −30.9 ‰ to −11.0 ‰ and −26.8 ‰ to −22.0 ‰, respectively. Pyrite in DT119A shows patchy zonation in Co and Ni with relatively low intragrain variability (Figures 6a–6c). In contrast, each of the three pyrite grains analyzed in sample K12 display unique trace element zoning and isotopic patterns (Figure S11): (1) patchy zoning of Co and As with a −30.9 ‰ core and −30.6 ‰ rim; (2) oscillatory zoning of As and Ni, patchy zoning of Co, and variation in δ^{34}S from −31.9 ‰ to −31.0 ‰ across the grain; and (3) a central core surrounded by a high As, Co, and Ni annulus (Figures 7d–7f) with δ^{34}S values of −23.9 ‰ to −22.7 ‰ measured in the core and −13.3 ‰ to −11.0 ‰ measured in the mantle and rim.

Metasomatic sulfide grains in a calc-schist sample from the Austria (FT105B) display elevated δ^{34}S values ranging from +6.2 ‰ to +13.9 ‰. Isotopic variability of up to 4.2 ‰ roughly corresponds with oscillatory zoning of Co and patchy zoning of Ni + Co. A transect across the largest grain displays an increase from +11.5 ± 0.1 ‰ in the core to +13.9 ± 0.2 ‰ in the mantle, followed by a decrease to +9.8 ± 0.2 ‰ at the rim (Figure 6b).

4.3. Mixed-Composition Samples

Metasomatic sulfides in rocks of mixed-composition (blackwall) display a large variation in sulfur isotopes, ranging from −21.7 ‰ to +12.5 ‰. Analyses of pyrite in jadeitite from the Dominican Republic (DR1203-07-02) display core to rim variations of up to 14.7 ‰ within single grains (Figure S10). These cores show elevated δ^{34}S (up to 12.5 ‰ higher) relative to rims and are encompassed by xenoblastic to idioblastic high-Co annuli. Pyrite in other samples exhibits cyclic zoning in Co (SY404, D1203-15-02) or both Co and As (PMQ-065). Significant isotopic variation is displayed across these grains. In sample PMQ-065, δ^{34}S values increase from −9.0 ‰ in the high-Co core to −7.7 ‰ in the low-Co mantle and a steady decrease to −8.3 ‰ in the rim (Figure 6c). Similarly, a core-to-rim transect of a pyrite grain in sample SY404 reveals an
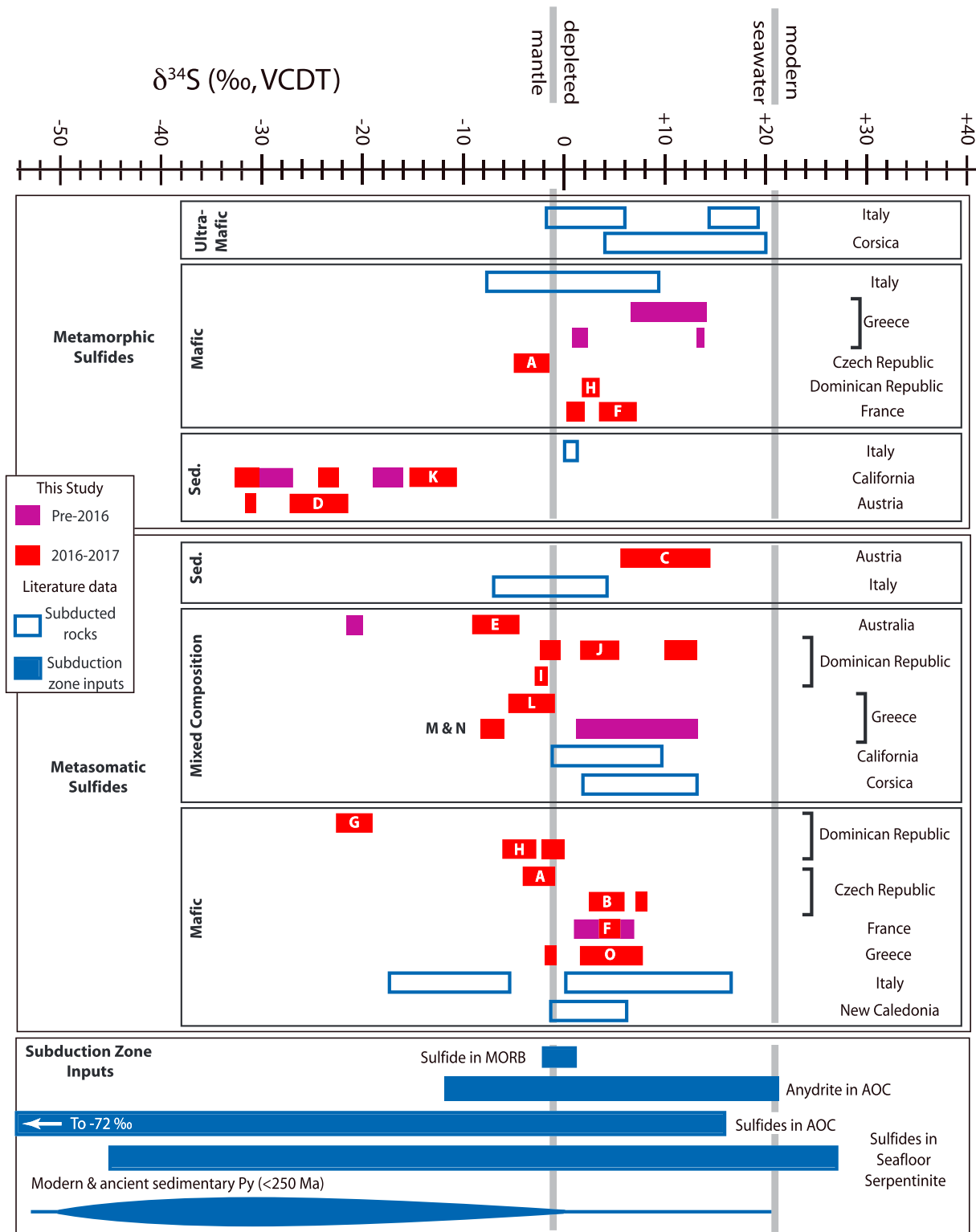
Figure 4. Upper panel: In situ and single-grain sulfur isotope data (δ^{34}S, ‰) from this study of metamorphic and metasomatic sulfide from high-pressure metamorphic rocks. Letters refer to each sample as described in Table 2. Data in open boxes from Bebout (1995), Crossley et al. (2018), Evans et al. (2014), Giacometti et al. (2014), and Shimizu et al. (2013). Lower panel: Summary of sulfur isotope compositions of seafloor rocks. Where sufficient data exist, the width of bars refers to distribution of sulfur isotopes in a given lithology. Data are from Alford et al. (2011), Alt (1995), Alt et al. (2013), Alt & Shanks (2011), Canfield & Farquhar (2009), Labidi et al. (2013, 2014), Ono et al. (2012), and Rouxel et al. (2008). VCDT = Vienna Canyon Diablo Troilite.
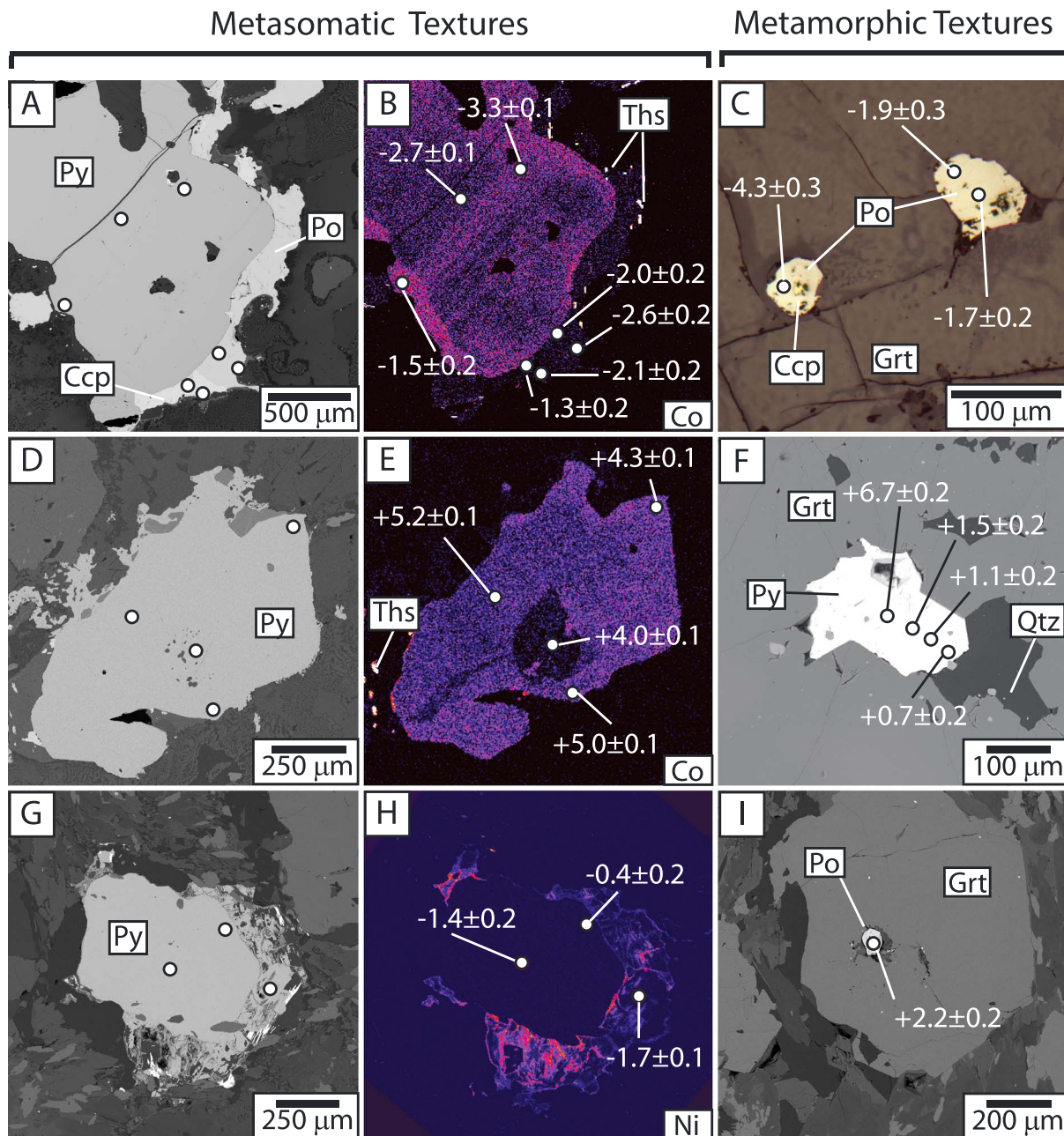
Figure 5. Reflected light images, backscattered-electron images, and trace element maps of metamorphic and metasomatic sulfides in metabasic samples SVS-11-01 (a–c), G08-12 (d–f), and DR1203-11-03 (g–i). Locations of sulfur isotope analyses are plotted (dots) with corresponding δ^{34}S values and 2SE. Thiospinel (Ths) grains are visible in cobalt maps (b and e).

increase from -4.5 ± 0.1 ‰ in the core to -1.5 to -0.9 ‰ in the mantle, followed by a decrease to -3.3 ± 0.1 ‰ in the rim (Figure 6d).

5. Discussion

Sulfur isotope data are categorized texturally and lithologically (Figure 4) to illustrate key isotopic trends. These data represent the largest compilation of sulfur isotope analyses to date for the subducted oceanic lithosphere. Isotopic differences are expected between disparate bulk rock compositions at the seafloor and these differences may be preserved during prograde metamorphism. Additionally, the isotopic
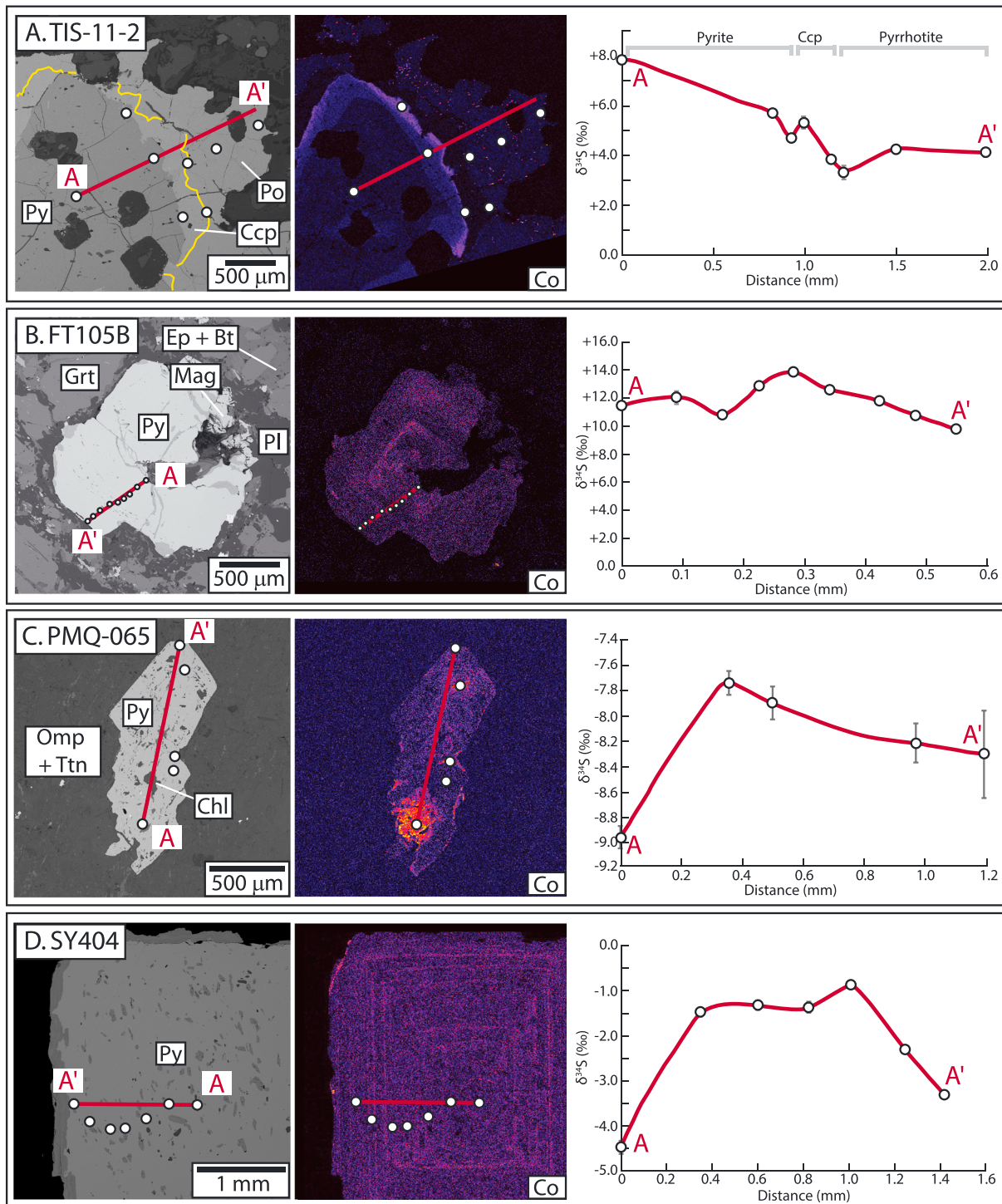
Figure 6. Sulfur isotope transects of metasomatic sulfides with corresponding backscattered-electron images and trace element maps for samples TIS-11-02 (a), FT105B (b), PMQ-065 (c), and SY404 (d). Transects are labeled from A to A′, and error bars are 2SE analytic uncertainty. The yellow line in panel (a) marks the chalcopyrite-pyrrhotite grain boundary.

compositions of sulfides formed during exhumation may reflect the mixing of isotopically distinct slab sources and fractionation during sulfide precipitation. To assess the breadth of sulfur isotope variability during subduction, it is necessary to consider the relationships of sulfide textures and trace element zoning with protolith composition and age.
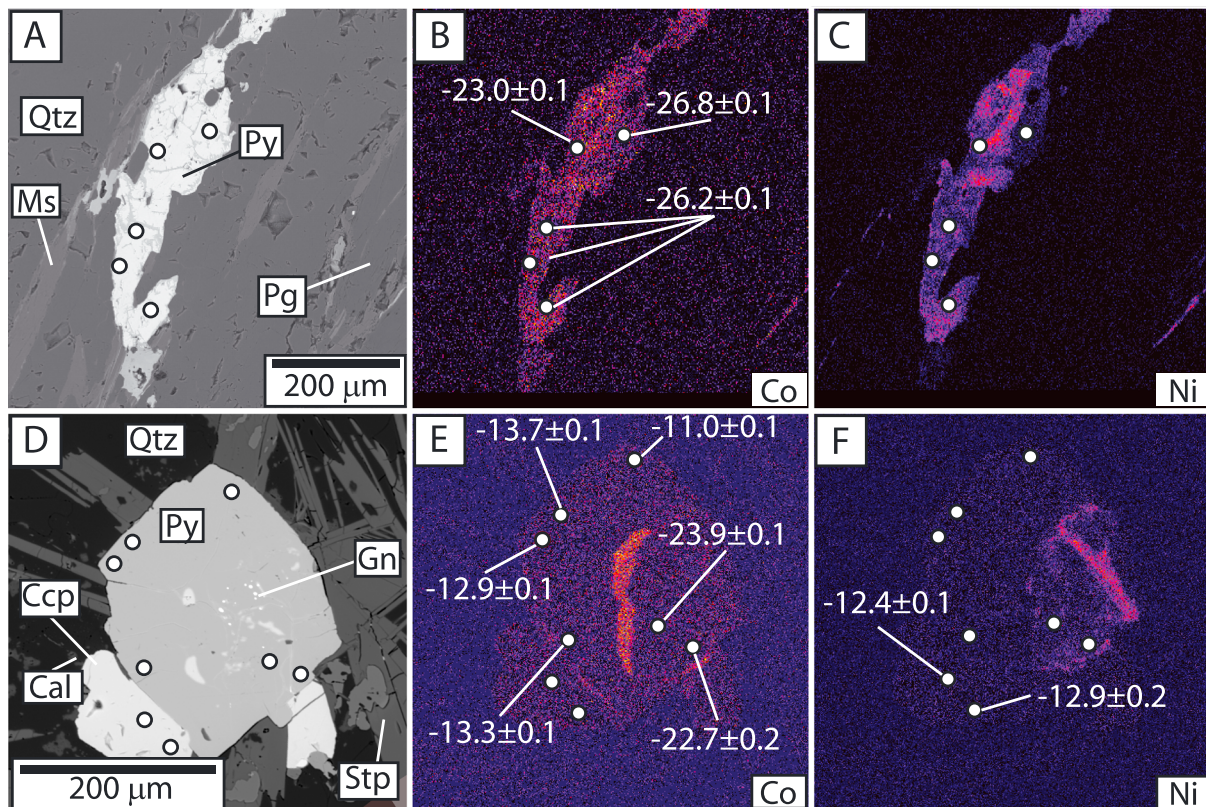
Figure 7. Back scattered electron images and trace element maps of metamorphic sulfides in metasedimentary samples DT119A (a–c) and K12 (d–f). Locations of sulfur isotope analyses are plotted (dots) with corresponding $\delta^{34}S$ values and 2SE.

5.1. Sulfur-Liberating Reactions and Sulfur Speciation in Slab Fluids
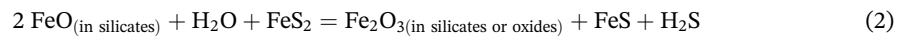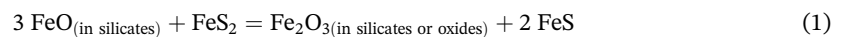
Compared to regional metamorphic settings, relatively few studies have examined the chemical reactions driving sulfur loss within subduction slabs. Currently, both reduced (H_2S, HS^-, and S_3^-) and oxidized species (SO_4^{2-}) species have been proposed to occur under subduction zone conditions (e.g., Benard et al., 2018; Evans et al., 2014; Philippot & Selverstone, 1991; Pokrovski & Dubrovinsky, 2011). In the presence of pyrite, the solubilities of reduced species are expected to be low (10^{-3}–10^{-5} m) compared to sulfate (>0.3 m) depending on P-T, pH, fO_2, and salinity (Evans et al., 2014; Newton & Manning, 2005). Additionally, sulfide mineral-fluid fractionation is expected to be 1–2 orders of magnitude higher for dissolved SO_4^{2-} than for H_2S and HS^- (Ohmoto & Rye, 1979). Therefore, identification of sulfur-liberating reactions and the resulting fluid speciation are critical to both the efficacy of sulfur loss from the slab and the interpretation of sulfur isotope data from exhumed terranes and active margins.

Sulfides are common accessory minerals in the oceanic crust, and their breakdown during high-pressure metamorphism would drive sulfur loss from subducting slabs. Pyrite is the dominant sulfide in the mafic oceanic crust, where pyrite and minor Fe-Cu-Ni sulfides of varying oxidation state replace igneous Fe-Cu-Ni monosulfides during seafloor alteration (e.g., Alford et al., 2011; Alt & Shanks, 1998, 2011; Alt et al., 1989, 2007, 2010). Pyrite is also the dominant sulfide in seafloor sediments (see review in Schoonen, 2004).

Sulfates also occur in the oceanic crust and sedimentary cover and may play a role in the isotopic composition and fO_2 of slab fluids. Anhydrite may be mobilized as pore water is released at the onset of subduction over the 100–250 °C temperature range. Tomkins and Evans (2015) argue that the retrograde solubility of anhydrite at low pressure drives reprecipitation of anhydrite in the upper portion of the slab as fluids encounter a mantle-driven inverted thermal gradient; however, no thermomechanical models predict an inverted gradient in the shallow part of subduction zones at 100–250 °C (e.g., Gerya et al., 2002; Syracuse et al., 2010). Additionally, the solubility of anhydrite at 100–200 °C ranges from 0.015 to 0.025 mol/kgH$_2$O

in the $CaSO_4$-$NaCl$-H_2O system (Freyer & Voigt, 2004). Jarrard (2003) estimated 3.29×10^{11} kg/year of pore fluid loss from AOC globally, which would result in 4.9–8.2×10^9 mol/year of anhydrite loss due to pore fluid expulsion. By subtracting our estimated pore fluid anhydrite flux from the $\sim5.1 \times 10^{11}$ mol/year of sulfate subduction estimated by Evans (2012), we estimate that only $\leq1.6\%$ of anhydrite is lost to pore fluid expulsion. Despite these estimates for anhydrite retention, the authors are unaware of any studies reporting anhydrite inclusions associated with early prograde subduction metamorphism; therefore, the role that anhydrite inherited from the seafloor plays during high-pressure metamorphism remains unclear.
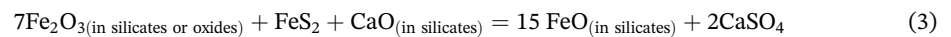
Reactions of pyrite to pyrrhotite are commonly observed with increasing metamorphic grade during regional metamorphism of metasedimentary rocks (e.g., Ferry, 1981; Guidotti, 1970; Nesbitt, 1982; Thompson, 1972; Tracy & Robinson, 1988) and are postulated by Tomkins and Evans (2015) to occur also during high-pressure metamorphism. In the FeO–SiO_2–$S_2\pm H_2O$ systems, reactions of pyrite to pyrrhotite may take the generalized form:

$$3\,FeO_{\text{(in silicates)}} + FeS_2 = Fe_2O_{3\text{(in silicates or oxides)}} + 2\,FeS \tag{1}$$

$$2\,FeO_{\text{(in silicates)}} + H_2O + FeS_2 = Fe_2O_{3\text{(in silicates or oxides)}} + FeS + H_2S \tag{2}$$

Reactions (1) and (2) exhibit some defining characteristics. First, reduction of one mole of S^- to S^{2-} is balanced by the oxidation of one mole of Fe^{2+} to Fe^{3+} in silicates. Conservation of sulfur requires a twofold increase of iron in the sulfide phase, and iron is scavenged from silicates. As a consequence, Fe-depleted and Mg-, K-, and Al-enriched assemblages are commonly observed as a result of pyrite breakdown to pyrrhotite in metamorphosed ore deposits (e.g., Nesbitt, 1982; Tomkins & Grundy, 2009). Thus, pyrite breakdown to pyrrhotite reactions operating during subduction metamorphism should produce oxidized Fe-depleted peak mineral assemblages in exhumed high-pressure rocks. Additionally, the low solubility of reduced sulfur species in rock-buffered systems suggests that sulfides may continue to persist in the slab (Evans et al., 2014; Giacometti et al., 2014; Tomkins & Evans, 2015).

Our textural observations are inconsistent with Reactions (1) and (2). We observe a decrease in ferric-iron bearing phases, such as chlorite, amphibole, and epidote, during prograde metamorphism, consistent with Reaction (3), whereas Reactions (1) and (2) would require an increase in bulk rock $Fe^{3+}/\Sigma Fe$. More importantly, sulfides are likely to persist as pyrrhotite in Reactions (1) and (2). This is not observed; matrix sulfides are not texturally associated with prograde to peak metamorphic mineral assemblages, with the exception of two samples (K12 and DT119A).

In contrast to the models based on the reactions discussed above, we propose that breakdown of sulfides and sulfur loss in subducted mafic and sedimentary rocks are likely balanced by the reduction of ferric iron to ferrous iron:

$$7Fe_2O_{3\text{(in silicates or oxides)}} + FeS_2 + CaO_{\text{(in silicates)}} = 15\,FeO_{\text{(in silicates)}} + 2CaSO_4 \tag{3}$$

Reaction (3) will drive a decrease in oxidation budget in the bulk rock during prograde metamorphism: For every mole of S^- oxidized to S^{6+}, seven moles of Fe^{3+} are reduced to Fe^{2+}. Given the oxidized nature of AOC (e.g., >3 times higher $Fe^{3+}/\Sigma Fe$ than MORB for the upper volcanic section; Bach and Edwards, 2003), Reaction (3) is unlikely to be limited by a deficiency in the electron receptor (i.e., trivalent iron). Reactions of this type may occur concurrently with dehydration reactions, thus providing a vehicle for anhydrite dissolution and mobilization of oxidized sulfur in slab fluids. Reaction (3) is consistent with other studies which propose a flux of oxidized sulfur, as SO_4^{2-} or SO_2, in slab fluids and melts (e.g., Benard et al., 2018; Canil & Fellows, 2017; Debret et al., 2015, 2016; Debret & Sverjensky, 2017; Frezzotti et al., 2011; Pons et al., 2016). Similarly, new thermodynamic models of subducted sediment predict dissolved $CaSO_4$ in slab fluids (Connolly & Galvez, 2018). These studies are consistent with the observation of sulfate minerals within multiphase solid inclusions and as daughter crystals in fluid inclusions in subducted oceanic and continental crust (see Table 1 in Frezzotti & Fernando, 2015).

In two samples with matrix metamorphic sulfides, Reaction (3) is likely inhibited by the bulk composition. In sample DT119A, pyrite grains are elongate parallel to the peak eclogite-facies foliation and are texturally associated with peak metamorphic garnet growth (Figures 2 and 7; Hawkins et al., 2007). These observations

suggest pyrite stability at 540–584 °C (Dachs & Proyer, 2001), well within the temperature range observed for the pyrite to pyrrhotite reaction (Ferry, 1981; Guidotti, 1970; Nesbitt, 1982). Similarly, pyrite was found to be stable at *P-T* conditions of 1.9 GPa and 600 °C in eclogites from New Caledonia (Brown et al., 2014). Interestingly, the pyrite to pyrrhotite reaction is observed during retrograde metamorphism in two samples (TIS-11-02 and SVS-11-01). In these samples early retrograde pyrite is replaced by chalcopyrite, and pyrrhotite + thiopsinel (see section 2.2 and Figure 5). Sulfur reduction (S^- to S^{2-}) is balanced by the oxidation of Fe, Ni, and Co to produce chalcopyrite and thiopsinel. Large variations in FeS_2/FeS within rocks at similar *P-T* conditions highlights the dependence of bulk rock and fluid composition on the pyrite to pyrrhotite reaction (Ferry, 1981; Tracy & Robinson, 1988); however, our observations suggest that pressure may also play an important role in stabilizing pyrite to higher temperatures.

Sufficiently low bulk Fe or $Fe^{3+}/\Sigma Fe$ may prevent Reaction (3) from proceeding in some rocks and stabilize sulfides to higher *P-T*. An example of the former case is the low-bulk-Fe assemblage of spessartine + quartz in the quartzite sample K12 (Laytonville Quarry, CA), whereas the graphite rich inclusion trails in sample DT119 (Frosnitz Valley, AT) suggests relatively reducing conditions during prograde metamorphism. The presence of metamorphic matrix sulfides in both samples is consistent with the expected inhibition of Reaction (3) in these bulk compositions.

Metasomatic sulfide textures are consistent with rehydration by oxidized sulfur-bearing slab fluids during incorporation of blocks into the mélange slab-mantle interface and exhumation of the mélange. Our data suggest a shift to higher fO_2 during metasomatism, consistent with the reverse of Reaction (3). For example, the assemblage Grt + Omp + Czo + Rt is overprinted by the more oxidized assemblage Grt + Omp + Chl + Ilm + Py during blackwall formation on metagabbroic blocks on Syros (e.g., SY462). Similarly, sulfides in eclogites retrogressed through the granulite- and amphibolite-facies (SVS-11-01, TIS-11-02, G083-12) are associated with retrograde hornblende and chlorite replacing garnet and omphacite. In sample SVS-11-01, sulfides are texturally coeval with inclusions of magnetite replacing hercynite in hornblende and ilmenite replacing matrix rutile (see discussion in supporting information Text 1). Similarly, pyrite and chalcopyrite are associated with epidote and magnetite after garnet in a metasediment from the Frosnitz Valley (FT105B, Figures 2f and 6b).

All of these textures suggest that the reverse of Reaction (3) occurs during rehydration: The reduction of dissolved sulfate to form pyrite is balanced by the oxidation of iron. More importantly, these textures are observed in rocks of varying bulk composition, age, and setting, suggesting that oxidized sulfur-bearing slab fluids may be a widespread occurrence. The textural evidence provided here is compelling, and future studies coupling the determination of fO_2–fS_2 from mineral compositions to thermodynamic modeling are required to fully constrain the speciation of sulfur in slab fluids. As we cannot conclusively confirm oxidized sulfur-bearing fluids, further discussions of fractionation below still consider reduced (H_2S) as well as oxidized (SO_4^{2-}) endmembers.

5.2. Isotopic Composition of Subducting Oceanic Lithosphere

Here we attempt to provide a synthesis of the isotopic values of global high-pressure sulfides based on the variety of samples analyzed in this study. Sulfur isotopic data are considered on the basis of petrogenesis (metamorphic vs. metasomatic), host rock bulk composition, and protolith age. The data presented in Figure 4 display large variations in $\delta^{34}S$ values from the grain to terrane scale and highlight the importance of linking in situ sulfur isotope analyses with sulfide petrogenesis.

Metamorphic sulfides in mafic rocks display a relatively restricted range of isotopic compositions, with 75 % of $\delta^{34}S$ values ($n = 12$) falling between −5 ‰ and +5 ‰ (Figure 4). These values are consistent with those reported for AOC (including the sheeted dike and gabbro sections, where available), where 78 % of whole rock and sulfide analyses fall within −5 ‰ and +5 ‰ (Alford et al., 2011; Alt, 1995; Alt & Shanks, 2011; Ono et al., 2012; Rouxel et al., 2008). Although $\delta^{34}S$ values for AOC generally fall close to 0 ‰, the distribution generally covers ~55 ‰ (−29 ‰ to +25 ‰) and is skewed significantly to values below 0 ‰ ($\gamma/SE = -2.9$; Figure 4), though values as low as −72.4 ‰ have been observed in deeply buried mid-ocean ridge flank basalts (Lever et al., 2013). Sulfur isotope compositions >+10 ‰ for pyrite in garnet from Syros (sample SY403) are surprisingly high, but are consistent with the total range of $\delta^{34}S$ values reported for AOC. Giacometti et al. (2014) reported a ~21 ‰ range (−6.7 ‰ to +13.9 ‰) for metabasite-hosted sulfides in
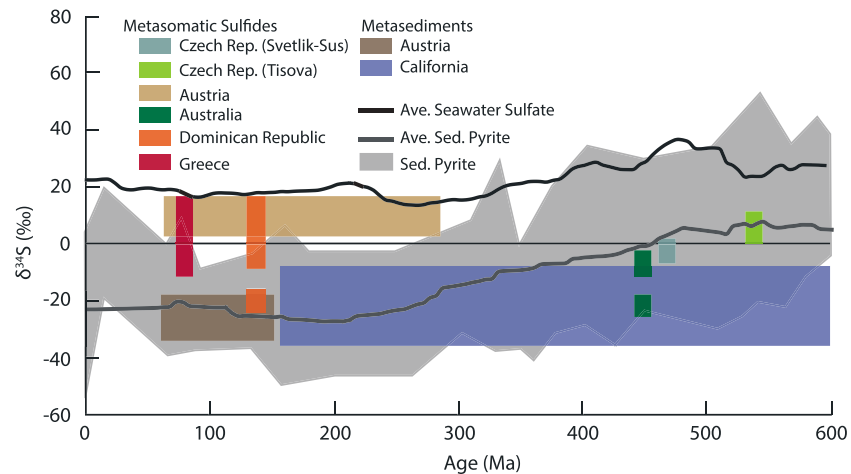
Figure 8. The range in δ^{34}S values of metasomatic and metasedimentary sulfides are plotted with respect to protolith age for different localities (see supporting information Text S1). The range (gray field) and moving average (dark gray curve) of sedimentary pyrite, as well as a moving average of seawater sulfate, are also plotted for comparison (after Canfield & Farquhar, 2009).

two metamorphosed ocean floor-related sulfide deposits in the Italian Western Alps. The data of Giacometti et al. (2014) largely cluster between 0 ‰ and +10 ‰, similar to sulfides in many modern mid-ocean ridge, back arc, and arc hydrothermal systems (e.g., Herzig et al., 1998; McDermott et al., 2015; Peters et al., 2010). These comparisons suggest that the seafloor character of δ^{34}S values of metamorphic sulfides in metabasic rocks are preserved throughout the metamorphic cycle.

Metamorphic sulfides in metasedimentary rocks commonly have negative δ^{34}S values (Figure 4). For the past ~250 Myr, the mean δ^{34}S value of sedimentary pyrite was just below −25 ‰ with a range from approximately −50 to +20 ‰ (Figure 8; Canfield & Farquhar, 2009). Nearly 94 % of all sulfur isotope analyses over this period fall below 0 ‰, and 68 % fall below −20 ‰ (Canfield & Farquhar, 2009). The sulfur isotope composition of metasedimentary sulfides in sample DT119 ranges from −31.1 ‰ to −21.0 ‰, consistent with the proposed Late-Mesozoic depositional age (between 145 and 66 Ma; Figure 8). In metasedimentary sample K12, δ^{34}S values of sulfides fall between −32.4 ‰ and −11.0 ‰. Although there are no estimates for the depositional age of sample K12, the distribution of δ^{34}S values is consistent with values of Early- to Mid-Mesozoic sedimentary pyrite (Figure 8).

In situ sulfur isotope measurements on metamorphic sulfides have been reported from Early to Mid-Mesozoic serpentinites metamorphosed to high-pressure conditions from Erro-Tobbio, Italy (−2 to +18 ‰; Shimizu et al., 2013) and Alpine Corsica (+1.9 to +10.3 ‰; Crossley et al., 2018). These data are consistent with whole rock δ^{34}S values of +6.9 ‰ to +14.3 ‰ and −3.5 ‰ to +9.7 ‰ from high-pressure serpentinite from the Erro-Tobbio, Italy, and Cerro del Almirez, Spain (Late Paleozoic protolith age), respectively (Alt, Shanks, et al., 2012, Alt, Garrido, et al., 2012). Sulfur isotope compositions of +5 ‰ to +10 ‰ and −45 ‰ to +27 ‰ have been reported for high- and low-temperature seafloor serpentinites, respectively (Alt et al., 2013). Therefore, high-pressure serpentinites tend to reflect some of the isotopic heterogeneity of seafloor serpentinites while tending toward positive delta values. These data, and those for mafic and sedimentary samples, suggest that protolith sulfur isotope compositions are preserved during high-pressure metamorphism.

5.3. The effects of Diffusion and Sulfur Speciation on Isotopic Fractionation

The rate of sulfur self-diffusion in sulfides will influence isotopic equilibrium and the ability for sulfur isotopes to faithfully record sulfide growth histories. Experimental data suggest that intracrystalline diffusion rates for sulfur atoms in sulfides are relatively rapid. For example, closure temperatures of 450 to 575 °C were calculated by Watson et al. (2009) for pyrite grains with radii of 200 μm to 1 mm at a cooling rate of 10 °C/Ma. These data suggest that partial relaxation of isotopic zoning is expected for sulfides in eclogite facies samples,

particularly in those with granulite and upper-amphibolite facies overprints (e.g., SVS-11-01, TIS-11-02, and G083-12-3).

In contrast, studies of metamorphosed pyrite have shown that $\delta^{34}S$ values remain undisturbed at metamorphic conditions up to the lower granulite facies (Alirezaei & Cameron, 2001; Bailie et al., 2010; Cook & Hoefs, 1997; Lange et al., 1993; Oliver et al., 1992; Wagner et al., 2004; Wagner & Boyce, 2006). Evans et al. (2014) and Giacometti et al. (2014) similarly reported minimal isotopic re-equilibration during subduction metamorphism on the basis of large intragrain isotopic variations over short length scales. These findings are consistent with our observations. For example, pyrite grains in eclogites retrogressed in the granulite and amphibolite facies from the Vendee (G083-12) show variation of up to ~6 ‰ on the scale of ~ 50 μm (Figures 5d–5f). Yet, based on the diffusion data of Watson et al. (2009), sulfur atoms should migrate distances of 50 μm in less than 1 Myr at 600 °C. Additionally, isotopic fractionations for pyrite-chalcopyrite pairs in all our samples are inconsistent with equilibrium, as evidenced by either reverse fractionation (higher ^{34}S pyrite relative to chalcopyrite) or unrealistic apparent sulfur isotope fractionation temperatures (see Table S24). Preservation of intragrain heterogeneities and isotopic disequilibrium among grains requires slower rates for sulfur self-diffusion in sulfides than experimentally determined. Therefore, it is reasonable to treat $\delta^{34}S$ values presented in this study as representative of sulfide growth.

We argue that slow diffusion of sulfur in sulfides prohibits fractionation during sulfur loss from the slab. Although ^{34}S may be favorable in the fluid, the dissolution rate outpaces the intragrain diffusion rates, such that the fluid inherits the isotopic composition of the dissolving grain margin. In this way, the $\delta^{34}S$ values of slab fluids likely reflect the unfractionated compositions of their sources. The effect of sluggish diffusion is likely negligible if reduced species dominate in the fluid, where fractionations are small (Δ_{Py-H_2S} =1.2–0.5 ‰ at 300–600 °C); however, large fractionations between sulfide minerals and dissolved sulfate (Δ_{Py-SO_4} =19.0–8.5 ‰ at 300–600 °C) may be significantly diminished (Ohmoto & Rye, 1979). Note that the influence of pH on isotope fractionation is not expected to play an important role under subduction zone metamorphic conditions and is not discussed here (Giacometti et al., 2014).

In contrast to sulfur loss, isotopic fractionation is likely to occur during the precipitation of metasomatic sulfides from slab-derived fluids. In addition to temperature and sulfur speciation, the mobility of sulfur atoms to the site of sulfide nucleation, through either diffusion or advection in the fluid, will impact the way isotopic fractionation is recorded during sulfide precipitation. In a closed system (see section 5.4), isotopic variations will develop along a linear equilibrium path if sulfur diffusion rates are sufficiently high in both the fluid and solid phases. Instead, we propose that sluggish intracrystalline diffusion of sulfur atoms will inhibit the isotopic exchange between grain interiors and the fluid. Closure of the precipitating sulfide facilitates the evolution of the isotopic composition of both the fluid and sulfide grain along a Rayleigh fractionation curve: At 300 °C and 1 % fluid remaining, pyrite precipitating from H_2S will be enriched by ~4 ‰ relative to the starting fluid composition, whereas pyrite precipitating from dissolved SO_4 will be enriched by ~68 ‰. The Rayleigh effect may not be recorded as isotopic zoning in the sulfide if the system is also open with respect to fluid, such that new external sulfur is constantly supplied. The lack of Rayleigh-like isotopic core-to-rim variations observed in metasomatic sulfide grains in this study (Figure 6) is consistent with a high flux of sulfur to nucleation sites. This occurs when the isotopic composition of the fluid is continuously replenished, resulting in steady-state fractionation. A similar model has been proposed to account for the boron isotopic composition of metasomatic tourmaline from mélange rocks from Greece (Marschall, Ludwig, et al., 2006). We therefore propose that equilibrium fractionation would reasonably approximate the $\delta^{34}S$ values of fluids estimated from metasomatic sulfide compositions.

5.4. Linking Slab Fluids and Metasomatic Sulfide Compositions

The isotopic composition of metasomatic sulfides formed during rehydration of high-pressure rocks or the formation of rocks of mixed composition at high pressures (e.g., jadeitite, omphacite-garnet-chlorite fels) may be used to gain information about the nature of sulfur in slab fluids, such as the mixing between various sulfur sources and the speciation of fluid-mobile sulfur. Here we consider the impact of sulfur speciation, fluid migration, phase separation, and diffusion on the fractionation of sulfur isotopes and the $\delta^{34}S$ values of metasomatic sulfides.

Table 3
Predicted Isotopic Compositions of Dissolved Sulfate in Equilibrium With Pyrite

Sample	Temperature (°C)	Pyrite composition (δ^{34}S, ‰)		Fluid composition (δ^{34}S, ‰)	
		low	high	low	high
FT105B	500	8.4	13.9	17.8	24.8
PMQ-065	350–450	−21.7	−5.3	−9.7	10.9
DR1203-07-02	320–450	−2.2	12.3	10.0	30.5
DR1203-10-02	200–400	−21.6	−19.3	−7.2	8.8
SY404	350–450	−4.5	10.3	7.7	26.8
SY328	350–451	−8.0	−6.1	4.1	10.1
SY523	350–452	2.9	4.7	15.2	21.1
SY462	350–453	1.3	13.5	10.9	23.7

Metamorphic sulfides in high-pressure rocks show a range in δ^{34}S values extending from −31 ‰ in metasediments to +18 ‰ in high-pressure serpentinites, overlapping with the 34.8 ‰ range measured in metasomatic sulfides (Figure 4). If S isotope fractionation is small, as expected for sulfide mineral precipitation from H_2S or HS^- (<1 ‰; Ohmoto & Lasaga, 1982), the range of metasomatic sulfide δ^{34}S values may simply reflect variation in protolith compositions. Protolith heterogeneities may be preserved in fluids in larger, more coherent slices of subducted oceanic lithosphere, such as the Frosnitz Valley and Tisová, where fluids are concentrated along narrow zones of structural weakness (e.g., Bebout & Barton, 2002; Breeding et al., 2004; John et al., 2004; Spandler et al., 2004, 2007). In contrast, high fluid:rock ratios and deformation in mélange zones at the slab-mantle interface drive the homogenization of isotopic and geochemical signatures (e.g., Bebout & Barton, 2002: Breeding et al., 2004; King et al., 2006, 2007; Marschall & Schumacher, 2012; Sorensen et al., 1997, Spandler et al., 2007). Therefore, the large variation of δ^{34}S values observed in mélange samples, such as the 33.4 ‰ range exhibited in samples from the Rio San Juan Complex (Figure 4), is unlikely to represent an inheritance of end-member protolith compositions.

Here we use the range of isotopic compositions for metamorphic sulfides (Figure 4) and the sulfur mass balance of Evans (2012) to estimate a range of δ^{34}S values of −11 ‰ to +8 ‰ for slab fluids (see supporting information Text S3). Our calculation assumes complete mixing between sedimentary, mafic, and ultramafic sources and that fractionation during sulfur loss from the slab is inhibited by slow intracrystalline diffusion of sulfur (see section 5.3). Seafloor anhydrite may be retained to depth and mobilized during metamorphic devolatilization. Assuming 1 % of anhydrite in AOC (Alt, 1995) and a composition of +21 ‰, the impact of anhydrite dissolution on the bulk isotopic composition of slab fluids is less than 0.5 ‰. The estimated range may be reflected in volcanic arc sulfur isotope data if slab-derived sulfur is present. Although data unaffected by fractionation during magma ascent and degassing are sparse, our estimated range is consistent with the range of −9 ‰ to +7 ‰ reported for melt inclusions from the Lesser Antilles Arc (Bouvier et al., 2008). The predicted range is also broadly consistent with metasomatic sulfide analyses, which largely fall between −10 ‰ and +10 ‰ (Figure 4), as might be expected if fluids are dominated by reduced sulfur species. However, significant excursions from the predicted range and small fluid-sulfide fractionations are difficult to reconcile with the situation in mélange zones, where fluid mixing is likely to be efficient. Instead, mechanisms such as phase separation or fractionation during reactive transport may be responsible for the observed isotopic heterogeneity.

In fluid systems with significant coexisting reduced and oxidized dissolved sulfur species, phase separation may drive sulfur isotope fractionation under subduction zone conditions. In upper-crustal systems, rapid changes in pressure may partition H_2, CH_4, and H_2S into a vapor phase, whereas species such as SO_4^{2-} and HSO_4^- are retained in a fluid phase (Drummond & Ohmoto, 1985). The increased ratio of SO_4^{2-} to H_2S in the fluid leads to a depletion of ^{34}S in the remaining H_2S, and lower δ^{34}S values of sulfides precipitated from H_2S in these fluids (Ohmoto, 1985; Ohmoto & Rye, 1979). A significant miscibility gap occurs in the $NaCl$-H_2O-CO_2 system under subduction zone *P-T* conditions (Newton & Manning, 2010), and reduced sulfur species may partition into a H_2O-CO_2 vapor, whereas oxidized species remain in the brine.

At slab temperatures, the impacts of phase separation on S isotope fractionation are expected to be small: Assuming 90 % H_2S loss from a fluid with H_2S:SO_4 of unity at 600 °C, the isotopic composition of H_2S in
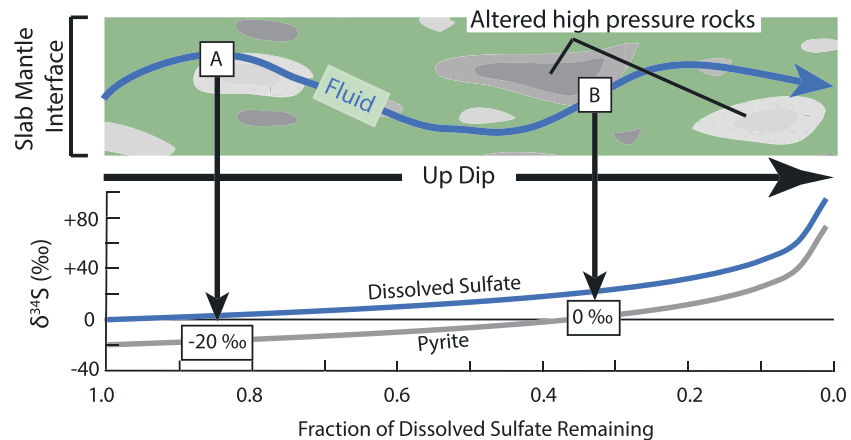
Figure 9. Schematic diagram illustrating the effect of Rayleigh distillation on dissolved sulfate and pyrite isotopic compositions during fluid migration at 300 °C. Pyrite precipitating near the fluid source (site A) will have a composition 20 ‰ lower than the fluid. Continued precipitation of pyrite as the fluid migrates produces elevated δ^{34}S values in the remaining fluid. For example, sulfides precipitating farther along the fluid pathway may have a composition of 0 ‰ (site B). Depending on the length of the path and the amount of pyrite precipitation, a range of up to 120 ‰ may be produced during fluid migration by this mechanism at 300 °C.

the brine is decreased by a maximum of ~2.4 ‰ relative to the starting composition (fractionation factors from Ohmoto & Lasaga, 1982). At 400 °C, the isotopic composition of H_2S decreases by up to ~3.9 ‰. The impact on the isotopic composition of the immiscible brine and vapor phases decreases dramatically at lower H_2S:SO_4. The authors are unaware of any fluid inclusion data which indicate reduced sulfur species in a vapor phase under subduction zone conditions (see review in Frezzotti & Fernando, 2015), suggesting that H_2S concentrations may be too low for unmixing to induce significant fractionation.

As an alternative, we propose that the large intrasample and intersample heterogeneity measured in metasomatic sulfides may be readily explained by sulfate-dominated fluids. Sulfide precipitation from sulfate-dominated fluids is consistent with our textural observations, in which metasomatic sulfides are associated with Fe^{3+}-bearing silicates $\pm$ oxides (see section 5.1). The isotopic compositions of sulfate-dominated fluids are calculated utilizing published *P-T* estimates for conditions estimated for metasomatic assemblages and are reported in Table 3. Isotopic compositions of sulfate-dominated fluids are calculated to be +11 ‰ to +24 ‰ higher than their corresponding sulfide analyses. For some samples, (e.g., PMQ-065 and DR1203-10-02), predicted fluid δ^{34}S values are consistent with the estimated range of −11 ‰ to +8 ‰ for slab fluids.

Dissolved sulfate compositions above +15 ‰ are unlikely to be directly produced by any slab source. To account for values >+15 ‰, we suggest a hypothetical reactive-transport model in which fluids migrate along the slab-mantle interface and precipitate sulfide minerals in exhuming high-grade blocks and mélange matrix. Sluggish intracrystalline diffusion of sulfur isotopes is expected to inhibit equilibration following sulfide precipitation. Continual sulfide precipitation and the lack of equilibration during fluid migration will drive the S remaining in the fluid to higher δ^{34}S along a Rayleigh distillation curve (Figure 9). In this way, sulfate-sulfide fractionation is capable of accounting for the entire range of δ^{34}S values measured in metasomatic sulfides. Again, a corresponding model has been invoked to explain the B isotope signature of tourmaline in mélange rocks from Syros (Marschall, Ludwig, et al., 2006). The validity of our model may be tested with in-depth spatial analysis of sulfur isotope variations within exhumed mélange zones.

6. Conclusions

In this paper we present a comprehensive sulfur isotope data set for sulfides in subduction terranes worldwide. These data demonstrate some broad global similarities for subducted sulfur through geologic time and highlight significant heterogeneities at the grain, sample, and terrane scales. Sulfides are broadly classified as metamorphic or metasomatic based on texture and chemistry. In metabasic rocks, metamorphic sulfides are generally only preserved as inclusions in prograde phases and δ^{34}S values between −5 ‰ and +5 ‰

are consistent with $\delta^{34}S$ values reported for AOC. Metamorphic sulfides in metasediments preserve a bacterial sulfate reduction signature (below −10 ‰). The sulfur isotope composition of metamorphic sulfides in high-pressure serpentinite samples range from −2 ‰ to +18 ‰ (Alt, Shanks, et al., 2012, Alt, Garrido, et al., 2012; Crossley et al., 2018; Shimizu et al., 2013) and are consistent with published data for seafloor serpentinite (Alt et al., 2013). These data suggest that sulfides preserved in high-pressure metamorphosed sedimentary, mafic, and ultramafic lithologies retain the sulfur isotopic composition of their protoliths.

Metasomatic sulfides are associated with textures consistent with the infiltration of oxidized sulfur-bearing fluids during exhumation, consistent with studies of fluid inclusions in high-pressure minerals (e.g., Frezzotti & Fernando, 2015), spinel-hosted melt inclusions from volcanic arcs (Benard et al., 2018), and thermodynamic models of subducted sediment (Connolly & Galvez, 2018). These sulfide grains exhibit a range of up to ~33 ‰ within individual exhumed terranes, and up to ~14 ‰ within individual grains. Although many metasomatic analyses range from −10 ‰ to +10 ‰, overlapping with the predicted range of −11 to +8 for slab fluids, the full range is difficult to account for without significant fractionation. Phase separation is unlikely to produce significant isotopic fractionation at the suspected low concentrations of H_2S in metasomatic fluids. Instead, we suggest that sluggish sulfur self-diffusion in sulfides prevents sulfide–fluid equilibration, a process expected to result in fluid $\delta^{34}S$ evolution along a Rayleigh distillation curve with distance from the source. As a result, higher $\delta^{34}S$ values are expected for metasomatic sulfides formed distally from the slab source and sulfate-sulfide fractionation can account for the entire isotopic range of metasomatic sulfides. This reactive transport hypothesis is consistent with the observed isotopic heterogeneities and mineral textures suggesting coupled Fe^{2+} oxidation and S^{6+} reduction during sulfide precipitation from slab fluids. Future thermodynamic modeling, petrographic analysis, and chemical studies of sulfur-liberating redox reactions during subduction will help to refine the evolution of the sulfur isotope system in slab-derived fluids.

References

Alford, S. E., Alt, J. C., & Shanks, W. C. (2011). Sulfur geochemistry and microbial sulfate reduction during low-temperature alteration of uplifted lower oceanic crust: Insights from ODP Hole 735B. *Chemical Geology*, *286*, 185–195.

Alirezaei, S., & Cameron, E. M. (2001). Variations of sulfur isotopes in metamorphic rocks from Bamble Sector, southern Norway: A laser probe study. *Chemical Geology*, *181*(1-4), 23–45. https://doi.org/10.1016/S0009-2541(01)00266-2

Alt, J. C. (1995). Sulfur isotopic profile through the oceanic crust: Sulfur mobility and seawater-crustal sulfur exchange during hydrothermal alteration. *Geology*, *23*(7), 585–588. https://doi.org/10.1130/0091-7613(1995)023<0585:SIPTTO>2.3.CO;2

Alt, J. C., Anderson, T. F., & Bonnell, L. (1989). The geochemistry of sulfur in a 1.3 km section of hydrothermally altered oceanic crust, DSDP 504B. *Geochimica et Cosmochimica Acta*, *53*(5), 1011–1023. https://doi.org/10.1016/0016-7037(89)90206-8

Alt, J. C., Garrido, C. J., Shanks, W. C., Turchyn, A., Padron-Navarta, J. A., Sanchez-Vizcaino, V. L., et al. (2012). Recycling of water, carbon, and sulfur during subduction of serpentinites: A stable isotope study of Cerro del Almirez, Spain. *Earth and Planetary Science Letters*, *327-328*, 50–60. https://doi.org/10.1016/j.epsl.2012.01.029

Alt, J. C., Laverne, C., Coggon, R. M., Teagle, D. A. H., Banerjee, N. R., Morgan, S., et al. (2010). Subsurface structure of a submarine hydrothermal system in oceanic crust formed at the East Pacific Rise, ODP/IODP Site 1256. *Geochemistry, Geophysics, Geosystems*, *11*, Q10010. https://doi.org/10.1029/2010GC003144

Alt, J. C., Schwarzenbach, E. M., Früh-Green, G. L., Shanks, W. C., Bernasconi, S. M., Garrido, C. J., et al. (2013). The role of serpentinites in cycling of carbon and sulfur: Seafloor serpentinization and subduction metamorphism. *Lithos*, *178*, 40–54. https://doi.org/10.1016/j.lithos.2012.12.006

Alt, J. C., & Shanks, W. C. (1998). Sulfur in serpentinized oceanic peridotites: Serpentinization processes and microbial sulfate reduction. *Journal of Geophysical Research*, *103*(B5), 9917–9929. https://doi.org/10.1029/98JB00576

Alt, J. C., & Shanks, W. C. (2006). Stable isotope compositions of serpentinite seamounts in the Mariana forearc: serpentinization processes, fluid sources and sulfur metasomatism. *Earth and Planetary Science Letters*, *242*(3-4), 272–285. https://doi.org/10.1016/j.epsl.2005.11.063

Alt, J. C., & Shanks, W. C. (2011). Microbial sulfate reduction and the sulfur budget for a complete section of altered oceanic basalts, IODP Hole 1256D (eastern Pacific). *Earth and Planetary Science Letters*, *310*(1-2), 73–83. https://doi.org/10.1016/j.epsl.2011.07.027

Alt, J. C., Shanks, W. C., Bach, W., Paulick, H., Garrido, C. J., & Beaudoin, G. (2007). Hydrothermal alteration and microbial sulfate reduction in peridotite and gabbro exposed by detachment faulting at the Mid-Atlantic Ridge, 15°20′N (ODP Leg 209): A sulfur and oxygen isotope study. *Geochemistry, Geophysics, Geosystems*, *8*, Q08002. https://doi.org/10.1029/2007GC001617

Alt, J. C., Shanks, W. C., Crispini, L., Gaggero, L., Schwarzenbach, E. M., Früh-Green, G. L., & Bernasconi, S. M. (2012). Uptake of carbon and sulfur during seafloor serpentinization and the effects of subduction metamorphism in Ligurian peridotites. *Chemical Geology*, *322-323*, 268–277. https://doi.org/10.1016/j.chemgeo.2012.07.009

Alt, J. C., Shanks, W. C., & Jackson, M. C. (1993). Cycling of sulfur in subduction zones—The geochemistry of sulfur in the Mariana-Island arc and back-arc trough. *Earth and Planetary Science Letters*, *119*(4), 477–494. https://doi.org/10.1016/0012-821X(93)90057-G

Aoyama, S., Nishizawa, M., Miyazaki, J., Shibuya, T., Ueno, Y., & Takai, K. (2018). Recycled Archean sulfur in the mantle wedge of the Mariana Forearc and microbrial sulfate reduction within an extremely alkaline serpentine seamount. *Earth and Planetary Science Letters*, *491*, 109–120. https://doi.org/10.1016/j.epsl.2018.03.002

Bach, W., & Edwards, K. J. (2003). Iron and sulfide oxidation within the basaltic ocean crust: Implications for chemolithoautotrophic microbial biomass production. *Geochimica et Cosmochimica Acta*, *67*(20), 3871–3887. https://doi.org/10.1016/s0016-7037(03)00304-1

Bailie, R. H., Gutzmer, J., Strauss, H., Stüeken, E., & McClung, C. (2010). Sulfur isotope characteristics of metamorphosed Zn-Cu volcanogenic massive sulfides in the Areachap Group, Northwestern Cape Province, South Africa. *Ore Geology Reviews*, *39*, 164–179.

Bebout, G. E. (1995). The impact of subduction-zone metamorphism on mantle-ocean chemical cycling. *Chemical Geology*, *126*(2), 191–218. https://doi.org/10.1016/0009-2541(95)00118-5

Bebout, G. E., & Barton, M. D. (1989). Fluid flow and metasomatism in a subduction zone hydrothermal system: Catalina Schist terrane, California. *Geology*, *17*(11), 976–980. https://doi.org/10.1130/0091-7613(1989)017<0976:FFAMIA>2.3.CO;2

Bebout, G. E., & Barton, M. D. (2002). Tectonic and metasomatic mixing in a high-T, subduction zone mélange – insights into the geochemical evolution of the slab-mantle interface. *Chemical Geology*, *187*(1-2), 79–106. https://doi.org/10.1016/S0009-2541(02)00019-0

Benard, A., Klimm, K., Woodland, A. B., Arculus, R. J., Wilke, M., Botcharnikov, R. E., et al. (2018). Oxidising agents in sub-arc mantle melts link slab devolatilisation and arc magmas. *Nature Communications*, *9*, 1–10.

Bottrell, S. H., & Newton, R. J. (2006). Reconstruction of changes in global sulfur cycling from marine sulfate isotopes. *Earth Science Reviews*, *75*(1-4), 59–83. https://doi.org/10.1016/j.earscirev.2005.10.004

Bouvier, A. S., Métrich, N., & Deloule, E. (2008). Slab-derived fluids in the magma sources of St. Vincent (Lesser Antilles Arc): volatile and light element imprints. *Journal of Petrology*, *49*(8), 1427–1448. https://doi.org/10.1093/petrology/egn031

Breeding, C. M., Ague, J. J., & Bröcker, M. (2004). Fluid-metasedimentary rock interactions in subduction-zone mélange: Implications for the chemical composition of arc magmas. *Geology*, *32*(12), 1041–1044. https://doi.org/10.1130/G20877.1

Brown, J. L., Christy, A. G., Ellis, D. J., & Arculus, R. J. (2014). Prograde sulfide metamorphism in blueschist and eclogite, New Caledonia. *Journal of Petrology*, *55*(3), 643–670. https://doi.org/10.1093/petrology/egu002

Cabral, R. A., Jackson, M. G., Rose-Koga, E. F., Koga, K. T., Whitehouse, M. J., Antonelli, M. A., et al. (2013). Anomolous sulphur isotopes in plume lavas reveal deep mantle storage of Archean crust. *Nature*, *496*(7446), 490–493. https://doi.org/10.1038/nature12020

Canfield, D. (2004). The evolution of the Earth Surface Sulfur Reservoir. *American Journal of Science*, *304*(10), 839–861. https://doi.org/10.2475/ajs.304.10.839

Canfield, D., & Farquhar, J. (2009). Animal evolution, bioturbation, and the sulfate concentration of the oceans. *Proceedings of the National Academy of Sciences*, *106*(20), 8123–8127. https://doi.org/10.1073/pnas.0902037106

Canil, D., & Fellows, S. A. (2017). Sulphide-sulphate stability and melting in subducted sediment and its role in arc mantle redox and chalcophile cycling in space and time. *Earth and Planetary Science Letters*, *470*, 73–86. https://doi.org/10.1016/j.epsl.2017.04.028

Cartigny, P., Farquhar, J., Thomassot, E., Harris, J. W., Wing, B., Masterson, A., et al. (2009). A mantle origin for Paleoarchean peridotite diamonds from the Panda kimberlite, Slave Craton: Evidence from ^{13}C-, ^{15}N- and ^{33,34}S-stable isotope systematics. *Lithos*, *1125*, 852–864.

Chaussidon, L., & Lorand, J. P. (1990). Sulfur isotope compositions of orogenic spinel lherzolite massifs from Ariege (North-Eastern Pyrenees, France): An ion microprobe study. *Geochimica et Cosmochimica Acta*, *54*(10), 2835–2846. https://doi.org/10.1016/0016-7037(90)90018-G

Chaussidon, M., Albarède, F., & Sheppard, S. M. F. (1987). Sulphur isotope heterogeneity in the mantle from ion microprobe measurements of sulphide inclusions in diamonds. *Nature*, *330*(6145), 242–244. https://doi.org/10.1038/330242a0

Chaussidon, M., Albarède, F., & Sheppard, S. M. F. (1989). Sulphur isotope variations in the mantle from ion microprobe analyses of micro-sulphide inclusions. *Earth and Planetary Science Letters*, *92*(2), 144–156. https://doi.org/10.1016/0012-821X(89)90042-3

Connolly, J. A. D., & Galvez, M. E. (2018). Electrolytic fluid speciation by Gibbs energy minimization and implications for subduction zone mass transfer. *Earth and Planetary Science Letters*, *501*, 90–102. https://doi.org/10.1016/j.epsl.2018.08.024

Cook, N. J., & Hoefs, J. (1997). Sulphur isotope characteristics of metamorphosed Cu-Pb-(Zn) volcanogenic massive sulfide deposits in the Norwegian Caledonides. *Chemical Geology*, *135*(3-4), 307–324. https://doi.org/10.1016/S0009-2541(96)00119-2

Crossley, R. J., Evans, K. A., Jeon, H., & Kilburn, M. R. (2018). Insights into sulfur cycling in subduction zones from in-situ isotope analysis of sulphides in high-pressure serpentinites and 'hybrid' samples from Alpine Corsica. *Chemical Geology*, *493*, 359–378. https://doi.org/10.1016/j.chemgeo.2018.06.014

Crowe, D. E., & Vaughan, R. G. (1996). Characterization and use of isotopically homogenous standards for in situ laser microprobe analysis of ^{34}S/^{32}S ratios. *American Mineralogist*, *81*(1-2), 187–193. https://doi.org/10.2138/am-1996-1-223

Dachs, E., & Proyer, A. (2001). Relics of high-pressure metamorphism from the Grossglockner region, Hohe Tauern, Austria: Paragenetic evolution and PT-paths of retrogressed eclogites. *European Journal of Mineralogy*, *13*(1), 67–86. https://doi.org/10.1127/0935-1221/01/0013-0067

de Hoog, J. C. M., Taylor, B. E., & van Bergen, M. J. (2001). Sulfur isotope systematics of basaltic lavas from Indonesia: Implications for the sulfur cycle in subduction zones. *Earth and Planetary Science Letters*, *189*(3-4), 237–252. https://doi.org/10.1016/S0012-821X(01)00355-7

Debret, B., Bolfan-Casanova, N., Padron-Navarta, J. A., Martin-Hernandez, F., Andreani, M., Garrido, C. J., et al. (2015). Redox state of iron during high=pressure serpentinite dehydration. *Contributions to Mineralogy and Petrology*, *169*, 1–18.

Debret, B., Millet, M. A., Pons, M. L., Bouilhol, P., Inglis, E., & Williams, H. (2016). Isotopic evidence for iron mobility during subduction. *Geology*, *44*(3), 215–218. https://doi.org/10.1130/G37565.1

Debret, B., & Sverjensky, D. A. (2017). Highly oxidizing fluids generated during serpentinite breakdown in subduction zones. *Scientific Reports*, *7*, 1–6.

Delevault, H., Chauvel, C., Thomassot, E., Devey, C. W., & Dazas, B. (2016). Sulfur and lead isotopic evidence of relic Archean sediments in the Pitcairn mantle plume. *Proceedings of the National Academy of Sciences*, *113*(46), 12952–12956. https://doi.org/10.1073/pnas.1523805113

Dreibus, G., & Palme, H. (1996). Cosmochemical Constraints on the sulphur content of the Earth's core. *Geochimica et Cosmochimica Acta*, *60*, 1125–1130.

Drummond, S. E., & Ohmoto, H. (1985). Chemical evolution and mineral deposition in boiling hydrothermal systems. *Economic Geology*, *80*(1), 126–147. https://doi.org/10.2113/gsecongeo.80.1.126

Eldridge, C. S., Compston, W., Williams, I. S., Harris, J. W., & Bristow, J. W. (1991). Isotope evidence for the involvement of recycled sediments in diamond formation. *Nature*, *353*(6345), 649–653. https://doi.org/10.1038/353649a0

Eldridge, C. S., Compston, W., Williams, I. S., Harris, J. W., Bristow, J. W., & Kinny, P. D. (1995). Applications of the SHRIMP I ion microprobe to the understanding of processes and timing of diamond formation. *Economic Geology*, *90*(2), 271–280. https://doi.org/10.2113/gsecongeo.90.2.271

Evans, K. A. (2012). The redox budget of subduction zones. *Earth-Science Reviews*, *113*(1-2), 11–32. https://doi.org/10.1016/j.earscirev.2012.03.003

Evans, K. A., & Powell, R. (2015). The effect of subduction on the sulphur, carbon and redox budget of lithospheric mantle. *Journal of Metamorphic Geology*, *33*(6), 649–670. https://doi.org/10.1111/jmg.12140

Evans, K. A., Reddy, S. M., Tomkins, A. G., Crossley, R. J., & Frost, B. R. (2017). Effects of geodynamic setting on the redox state of fluids released by subducted mantle lithosphere. *Lithos*, *278-281*, 26–42. https://doi.org/10.1016/j.lithos.2016.12.023

Evans, K. A., Tomkins, A. G., Cliff, J., & Fiorentini, M. L. (2014). Insights into subduction zone sulfur recycling from isotopic analysis of eclogite-hosted sulfides. *Chemical Geology*, *365*, 1–19. https://doi.org/10.1016/j.chemgeo.2013.11.026

Farquhar, J., Wing, B. A., McKeegan, K. D., Harris, J. W., Cartigny, P., & Thiemens, M. H. (2002). Mass-independent sulfur of inclusions in diamond and sulfur recycling on early Earth. *Science*, *298*, 2369–2372.

Faryad, S. W., Perraki, M., & Vrána, S. (2006). P-T evolution and reaction textures in retrogressed eclogites from Svetlik, the Moldanubian Zone (Czech Republic). *Mineralogy and Petrology*, *88*(1-2), 297–319. https://doi.org/10.1007/s00710-006-0142-8

Ferry, J. M. (1981). Petrology of graphitic sulfide-rich schists from south-central Maine: An example of desulfidation during prograde regional metamorphism. *American Mineralogist*, *66*, 908–930.

Freyer, D., & Voigt, W. (2004). The measurement of sulfate mineral solubilities in the Na-K-Ca-Cl-SO$_4$-H$_2$O system at temperatures of 100, 150 and 200°C. *Geochimica et Cosmochimica Acta*, *68*(2), 307–318. https://doi.org/10.1016/s0016-7037(03)00215-1

Frezzotti, M. L., & Fernando, S. (2015). The chemical behavior of fluids released during deep subduction based on fluid inclusions. *American Mineralogist*, *100*(2-3), 352–377. https://doi.org/10.2138/am-2015-4933

Frezzotti, M. L., Selverstone, J., Sharp, Z. D., & Compagnoni, R. (2011). Carbonate dissolution during subduction revealed by diamond-bearing rocks from the Alps. *Nature Geoscience*, *4*(10), 703–706. https://doi.org/10.1038/ngeo1246

Gao, X., & Thiemens, M. H. (1993a). Isotopic composition and concentration of sulfur in carbonaceous chondrites. *Geochimica et Cosmochimica Acta*, *57*(13), 3159–3169. https://doi.org/10.1016/0016-7037(93)90300-L

Gao, X., & Thiemens, M. H. (1993b). Variations in the isotopic composition of sulfur in enstatite and ordinary chondrites. *Geochimica et Cosmochimica Acta*, *57*(13), 3171–3176. https://doi.org/10.1016/0016-7037(93)90301-C

Gerya, T. V., Stockhert, B., & Perchuk, A. L. (2002). Exhumation of high-pressure metamorphic rocks in a subduction channel: A numerical simulation. *Tectonics*, *21*(6), 1056. https://doi.org/10.1029/2002TC001406

Giacometti, F., Evans, K. A., Rebay, G., Cliff, J., Tomkins, A. G., Rossetti, P., et al. (2014). Sulfur isotope evolution in sulfide ores from Western Alps: Assessing the influence of subduction-related metamorphism. *Geochemistry, Geophysics, Geosystems*, *15*, 3808–3829. https://doi.org/10.1002/2014GC005459

Giuliani, A., Fiorentini, M. L., Martin, L. A. J., Farquhar, J., Phillips, D., Griffin, W. L., & LaFlamme, C. (2016). Sulfur isotope composition of metasomatized mantle xenoliths from the Bultfontein kimberlite (Kimberley, South Africa): Contribution from subducted sediments and the effect of sulfide alteration on S isotope systematics. *Earth and Planetary Science Letters*, *445*, 114–124. https://doi.org/10.1016/j.epsl.2016.04.005

Guidotti, C. V. (1970). The mineralogy and petrology of the transition from the lower to upper sillimanite zone in the Oquossoc Area, Maine. *Journal of Petrology*, *11*(2), 277–336. https://doi.org/10.1093/petrology/11.2.277

Hacker, B. (2008). H$_2$O subduction beyond arcs. *Geochemistry, Geophysics, Geosystems*, *9*, Q03001. https://doi.org/10.1029/2007GC001707

Hawkins, A. T., Selverstone, J., Brearley, A. J., Beane, R. J., Ketcham, A., & Carlson, W. D. (2007). Origin and mechanical significance of honeycomb garnet in high-pressure metasedimentary rocks from the Tauern Window, Eastern Alps. *Journal of Metamorphic Geology*, *25*(5), 565–583. https://doi.org/10.1111/j.1525-1314.2007.00714.x

Hermann, J., Spandler, C., Hack, A., & Korsakov, A. V. (2006). Aqueous fluids and hydrous melts in high-pressure and ultra-high pressure rocks: Implications for element transfer in subduction zones. *Lithos*, *92*(3-4), 399–417. https://doi.org/10.1016/j.lithos.2006.03.055

Herzig, P. M., Petersen, S., & Hannington, M. D. (1998). Geochemistry and sulfur-isotopic composition of the TAG hydrothermal mound, Mid-Atlantic Ridge, 26°N'. *Proceeding of the Ocean Drilling Program, Scientific Results*, *158*, 47–70.

Ionov, D. A., Hoefs, J., Wedepohl, K. H., & Wiechert, U. (1992). Content and isotopic composition of sulphur in ultramafic xenoliths from central Asia. *Earth and Planetary Science Letters*, *111*(2-4), 269–286. https://doi.org/10.1016/0012-821X(92)90184-W

Jarrard, R. D. (2003). Subduction fluxes of water, carbon dioxide, chlorine, and potassium. *Geochemistry, Geophysics, Geosystems*, *4*(5), 8905. https://doi.org/10.1029/2002GC000392

Jego, S., & Dasgupta, R. (2013). Fluid-present melting of sulfide-bearing ocean-crust: Experimental constraints on the transport of sulfur from subducting slab to mantle wedge. *Geochimica et Cosmochimica Acta*, *110*, 106–134. https://doi.org/10.1016/j.gca.2013.02.011

John, T., Scherer, E. E., Haase, K., & Schenk, V. (2004). Trace element fractionation during fluid-induced eclogitization in a subducting slab: trace element and Lu-Hf-Sm-Nd isotope systematics. *Earth and Planetary Science Letters*, *227*(3-4), 441–456. https://doi.org/10.1016/j.epsl.2004.09.009

King, R. L., Bebout, G. E., Grove, M., Moriguti, T., & Nakamura, E. (2007). Boron and lead isotope signatures of subduction-zone mélange formation: Hybridization and fractionation along the slab-mantle interface beneath volcanic fronts. *Chemical Geology*, *239*(3-4), 305–322. https://doi.org/10.1016/j.chemgeo.2007.01.009

King, R. L., Bebout, G. E., Moriguti, T., & Nakamura, E. (2006). Elemental mixing of systematics and Sr-Nd isotope geochemistry of mélange formation: Obstacles to identification of fluid sources to arc volcanics. *Earth and Planetary Science Letters*, *246*(3-4), 288–304. https://doi.org/10.1016/j.epsl.2006.03.053

Kyser, T. K. (1990). Stable isotopes in the continental lithospheric mantle. *Reviews in Mineralogy and Geochemistry*, *16*, 131–164.

Labidi, J., Cartigny, P., Birck, J. L., Assayag, N., & Bourrand, J. J. (2012). Determination of multiple sulfur isotopes in glasses: A repraisal of the MORB δ^{34}S. *Chemical Geology*, *334*, 189–198. https://doi.org/10.1016/j.chemgeo.2012.10.028

Labidi, J., Cartigny, P., Hamelin, C., Moreira, M., & Dosso, L. (2014). Sulfur isotope budget (^{32}S, ^{33}S, ^{34}S, and ^{36}S) in Pacific-Antarctic ridge basalts: A record of mantle source heterogeneity and hydrothermal sulfide assimilation. *Geochimica et Cosmochimica Acta*, *133*, 47–67. https://doi.org/10.1016/j.gca.2014.02.023

Labidi, J., Cartigny, P., & Moreira, M. (2013). Non-chondritic sulphur isotope composition of the terrestrial mantle. *Nature*, *501*(7466), 208–211. https://doi.org/10.1038/nature12490

LaFlamme, C., Fiorentini, M. L., Lindsay, M. D., & Bui, T. H. (2018). Atmospheric sulfur is recycled to the crystalline continental crust during supercontinent formation. *Nature Communications*, *9*(1), 4380. https://doi.org/10.1038/s41467-018-06691-3

Lange, I. M., Nokleberg, W. J., Newkirk, S. R., Aleinikoff, J. N., Church, S. E., & Krouse, H. R. (1993). Devonian volcanogenic massive sulfide deposits and occurrences, southern Yukon-Tanana Terrance, eastern Alaska Range, Alaska. *Economic Geology*, *88*(2), 344–376. https://doi.org/10.2113/gsecongeo.88.2.344

Lee, C., Erdman, M., Yang, W., Ingram, L., Chin, E. J., & DePaolo, D. J. (2018). Sulfur isotopic composition of deep arc cumulates. *Earth and Planetary Science Letters*, *500*, 76–85. https://doi.org/10.1016/j.epsl.2018.08.017

Lever, M. A., Rouxel, O., Alt, J. C., Shimizu, N., Ono, S., Coggon, R. M., et al. (2013). Evidence for microbial carbon and sulfur cycling in deeply buried ridge flank basalt. *Science*, *339*(6125), 1305–1308. https://doi.org/10.1126/science.1229240

Mandeville, C. W., Sasaki, A., Saito, G., Faure, K., King, R., & Hauri, E. (1998). Open-system degassing of sulfur from Krakatau 1883 magma. *Earth and Planetary Science Letters*, *160*(3-4), 709–722. https://doi.org/10.1016/S0012-821X(98)00122-8

Mandeville, C. W., Webster, J. D., Tappen, C., Taylor, B. E., Timbal, A., Sasaki, A., et al. (2009). Stable isotope and petrologic evidence for open-system degassing during the climactic and pre-climactic eruptions of Mt. Mazama, Crater Lake, Oregon. *Geochimica et Cosmochimica Acta*, *73*(10), 2978–3012. https://doi.org/10.1016/j.gca.2009.01.019

Manning, C. E. (2004). The chemistry of subduction-zone fluids. *Earth and Planetary Science Letters*, *223*(1-2), 1–16. https://doi.org/10.1016/j.epsl.2004.04.030

Marini, L., Chiappini, V., Cioni, R., Cortecci, G., Dinelli, E., Principe, C., & Ferrara, G. (1998). Effect of degassing on sulfur contents and $\delta^{34}S$ values in Somma-Vesuvius magmas. *Bulletin of Volcanology*, *60*(3), 187–194. https://doi.org/10.1007/s004450050226

Marini, L., Moretti, R., & Accornero, M. (2011). Sulfur isotopes in magmatic-hydrothermal systems, melts, and magmas. *Reviews in Mineralogy and Geochemistry*, *73*(1), 423–492. https://doi.org/10.2138/rmg.2011.73.14

Marini, L., Paiotti, A., Principe, C., Ferrara, G., & Cioni, R. (1994). Isotopic ratio and concentration of sulphur in the undersaturated alkaline magmas of Vulture volcano (Italy). *Bulletin of Volcanology*, *56*(6-7), 487–492. https://doi.org/10.1007/BF00302829

Marschall, H. R., Ludwig, T., Altherr, R., Kalt, A., & Tonarini, S. (2006). Syros metasomatic tourmaline: Evidence for very high-$\delta^{11}B$ fluids in subduction zones. *Journal of Petrology*, *47*(10), 1915–1942. https://doi.org/10.1093/petrology/egl031

Marschall, H. R., & Schumacher, J. C. (2012). Arc magmas sourced from mélange diapirs in subduction zones. *Nature Geoscience*, *5*(12), 862–867. https://doi.org/10.1038/ngeo1634

McDermott, J. M., Ono, S., Tivey, M. K., Seewald, J. S., Shanks, W. C., & Solow, A. R. (2015). Identification of sulfur sources and isotopic equilibria in submarine hot-springs using multiple sulfur isotopes. *Geochimica et Cosmochimica Acta*, *160*, 169–187. https://doi.org/10.1016/j.gca.2015.02.016

Nesbitt, B. E. (1982). Metamorphic sulfide-silicate equilibria in the massive sulfide deposits at Ducktown, Tennessee. *Economic Geology*, *77*(2), 364–378. https://doi.org/10.2113/gsecongeo.77.2.364

Newton, R. C., & Manning, C. E. (2005). Solubility of anhydrite, $CaSO_4$, in $NaCl-H_2O$ solutions at high pressures and temperatures: Applications to fluid-rock interaction. *Journal of Petrology*, *46*, 701–716.

Newton, R. C., & Manning, C. E. (2010). Role of saline fluids in deep-crustal and upper mantle metasomatism: Insights from experimental studies. *Geofluids*, *10*, 58–72.

O'Brien, P. J. (1997). Garnet zoning and reaction textures in overprinted eclogites, Bohemian Massif, European Variscides: A record of their thermal history during exhumation. *Lithos*, *41*(1-3), 119–133. https://doi.org/10.1016/S0024-4937(97)82008-7

Ohmoto, H. (1985). Stable isotope geochemistry of ore deposits. *Reviews in Mineralogy and Geochemistry*, *222*, 436–446.

Ohmoto, H., & Lasaga, A. C. (1982). Kinetics of reactinos between aqueous sulfates and sulfides in hydrothermal systems. *Geochimica et Cosmochimica Acta*, *46*(10), 1727–1745. https://doi.org/10.1016/0016-7037(82)90113-2

Ohmoto, H., & Rye, R. O. (1979). Isotopes of sulfur and carbon. In H. L. Barnes (Ed.), *Geochemistry of Hydrothermal Ore Deposits*, (pp. 517–611). New York: Wiley.

Oliver, N. H. S., Hoering, T. C., Johnson, T. W., Rumble, D., & Shanks, W. C. (1992). Sulfur isotopic disequilibrium and fluid-rock inter- action during metamorphism of sulfidic black shales from the Waterville-Augusta area, Maine, USA. *Geochimica et Cosmochimica Acta*, *56*(12), 4257–4265. https://doi.org/10.1016/0016-7037(92)90266-L

Ono, S., Keller, N. S., Rouxel, O., & Alt, J. C. (2012). Sulfur-33 constraints on the origin of secondary pyrite in altered oceanic basement. *Geochimica et Cosmochimica Acta*, *87*, 323–340. https://doi.org/10.1016/j.gca.2012.04.016

Peters, M., Strauss, H., Farquhar, J., Ockert, C., Eickmann, B., & Jost, C. L. (2010). Sulfur cycling at the Mid-Atlantic Ridge: A multiple sulfur isotope approach. *Chemical Geology*, *269*(3-4), 180–196. https://doi.org/10.1016/j.chemgeo.2009.09.016

Philippot, P., & Selverstone, J. (1991). Trace-element-rich brines in elogitic veins: Implications for fluid composition and transport during subduction. *Contributions to Mineralogy and Petrology*, *106*(4), 417–430. https://doi.org/10.1007/BF00321985

Pokrovski, G. S., Borisova, A. Y., & Harrichoury, J. C. (2008). The effect of sulfur on vapor-liquid fractionation of metals in hydrothermal systems. *Earth and Planetary Science Letters*, *266*(3-4), 345–362. https://doi.org/10.1016/j.epsl.2007.11.023

Pokrovski, G. S., & Dubrovinsky, L. S. (2011). The S_3^- ion is stable in geological fluids at elevated temperatures and pressures. *Science*, *331*(6020), 1052–1054. https://doi.org/10.1126/science.1199911

Pokrovski, G. S., Kokh, M. A., Guillaume, D., Borisova, A. Y., Gisquet, P., Hazemann, J. L., et al. (2015). Sulfur radical species form gold deposits on Earth. *Proceedings of the National Academy of Sciences*, *112*(44), 13484–13489. https://doi.org/10.1073/pnas.1506378112

Pons, M. L., Debret, B., Bouihol, P., Delacour, A., & Williams, H. (2016). Zinc isotope evidence for sulfate-rich fluid transfer across sub- duction zones. *Nature Communications*, *7*(1), 13794. https://doi.org/10.1038/ncomms13794

Rees, C., Jenkins, W., & Monster, J. (1978). The sulphur isotopic composition of seawater sulphate. *Geochimica et Cosmochimica Acta*, *42*(4), 377–381. https://doi.org/10.1016/0016-7037(78)90268-5

Robinson, B. W., & Graham, I. J. (1992). The sulfur isotopic composition of mafic-intermediate volcanic rocks, Taupo Volcanic Zone, New Zealand. In Y. Kharaka, & A. Maest (Eds.), *Water-Rock Interaction*, (Vol. 7, pp. 975–978). Rotterdam, Netherlands: Balkema.

Rouxel, O., Ono, S., Alt, J. C., Rumble, D., & Ludden, J. (2008). Sulfur isotope evidence for microbial sulfate reduction in altered oceanic basalts at ODP Site 801. *Earth and Planetary Science Letters*, *268*(1-2), 110–123. https://doi.org/10.1016/j.epsl.2008.01.010

Rudnick, R. L., Eldridge, C. S., & Bulanova, G. P. (1993). Diamond growth history from in situ measurement of Pb and S isotopic compo- sitions of sulfide inclusions. *Geology*, *21*(1), 13–16. https://doi.org/10.1130/0091-7613(1993)021<0013:DGHFIS>2.3.CO;2

Rye, R. O., Luhr, J. F., & Wasserman, M. D. (1984). Sulfur and oxygen isotopic systematics of the 1982 eruptions of El Chichon Volcano, Chiapas, Mexico. *Journal of Volcanology and Geothermal Research*, *23*(1-2), 109–123. https://doi.org/10.1016/0377-0273(84)90058-1

Sakai, H., Des Marais, D. J., Ueda, A., & Moore, J. G. (1984). Concentrations and isotope ratios of carbon, nitrogen, and sulfur in ocean-floor basalts. *Geochimica et Cosmochimica Acta*, *48*, 2433–2442.

Schmidt, M. W., & Poli, S. (2003). Generation of mobile components during subduction of oceanic crust. In R. L. Rudnick (Ed.), *Treatise on Geochemistry*, (Vol. 3, pp. 567–591). Oxford, England: Elsevier.

Schoonen, M. A. A. (2004). Mechanisms of sedimentary pyrite formation. *Geological Society of America Special Papers*, *379*, 117–134.

Seal, R. R. (2006). Sulfur isotope geochemistry of sulfide minerals. *Reviews in Mineralogy and Geochemistry*, *61*(1), 633–677. https://doi.org/10.2138/rmg.2006.61.12

Seo, J. H., Guillong, M., & Heinrich, C. A. (2009). The role of sulfur in the formation of magmatic-hydrothermal copper-gold deposits. *Earth and Planetary Science Letters*, *282*(1-4), 323–328. https://doi.org/10.1016/j.epsl.2009.03.036

Shimizu, N., Scambelluri, M., Santiago Ramos, D., & Tonarini, S. (2013). Boron and sulfur isotopic variations during subduction of hydrated lithosphere. *Mineralogical Magazine*, *77*, 2201.

Sorensen, S. S., Grossman, J. N., & Perfit, M. R. (1997). Phengite-hosted LILE-enrichment in eclogite and related rocks: Implications for fluid-mediated mass transfer in subduction zones and arc magmas. *Journal of Petrology*, *38*(1), 3–34. https://doi.org/10.1093/petroj/38.1.3

Spandler, C., Hermann, J., Arculus, R., & Mavrogenes, J. (2004). Geochemical heterogeneity and elemental mobility in deeply subducted oceanic crust: Insights from high-pressure mafic rocks from New Caledonia. *Chemical Geology*, *206*(1-2), 21–42. https://doi.org/10.1016/j.chemgeo.2004.01.006

Spandler, C., Hermann, J., Faure, K., Mavrogenes, J., & Arculus, R. (2007). The importance of talc and chlorite "hybrid" rocks for volatile recycling through subduction zones; Evidence from high-pressure subduction mélange of New Caledonia. *Contributions to Mineralogy and Petrology*, *155*, 181–198.

Spandler, C., & Pirard, C. (2013). Element recycling from subducting slabs to arc crust: A review. *Lithos*, *170-171*, 208–223. https://doi.org/10.1016/j.lithos.2013.02.016

Suppe, J., & Armstrong, R. L. (1972). Potassium-argon dating of Franciscan metamorphic rocks. *American Journal of Science*, *272*(3), 217–233. https://doi.org/10.2475/ajs.272.3.217

Syracuse, E. M., van Keken, P. E., & Abers, G. A. (2010). The global range of subduction zone thermal models. *Physics of the Earth and Planetary Interiors*, *183*(1-2), 73–90. https://doi.org/10.1016/j.pepi.2010.02.004

Thode, H. G., Monster, J., & Dunford, H. B. (1961). Sulfur isotope geochemistry. *Geochimica et Cosmochimica Acta*, *25*, 159–174.

Thomassot, E., Cartigny, P., Harris, J. W., Lorand, J. P., Rollion-Bard, C., & Chaussidon, M. (2009). Metasomatic diamond growth: A multi-isotope study (^{13}C, ^{15}N, ^{33}S, ^{34}S) of sulphide inclusions and their host diamonds from Jwaneng (Botswana). *Earth and Planetary Science Letters*, *282*(1-4), 79–90. https://doi.org/10.1016/j.epsl.2009.03.001

Thompson, J.B., Jr. (1972). Oxides and sulfides in regional metamorphism of pelitic schsits. Proceedings of the 24th International Geological Congress, 10, 27-35.

Tomkins, A. G., & Evans, K. A. (2015). Separate zones of sulfate and sulfide release from subducted mafic oceanic crust. *Earth and Planetary Science Letters*, *428*, 73–83. https://doi.org/10.1016/j.epsl.2015.07.028

Tomkins, A. G., & Grundy, C. (2009). Upper temperature limits of orogenic gold deposit formation: Constraints from the granulite hosted Griffin's Find deposit, Yilgarn Craton. *Economic Geology*, *104*(5), 669–685. https://doi.org/10.2113/gsecongeo.104.5.669

Tracy, R. J., & Robinson, P. (1988). Silicate-sulfide-oxide-fluid reactions in granulite-grade pelitic rocks, central Massachusetts. *American Journal of Science*, *288-A*, 45–74.

Tsai, H., Shieh, Y., & Meyers, H. O. A. (1979). Mineralogy and 34S/32S ratios of sulfides associated with kimberlite, xenoliths and diamonds. In F. R. Boyd, & H. O. A. Meyer (Eds.), *The mantle sample: Inclusion in kimberlites and other volcanics*, (Vol. 16, pp. 87–103). Washington, DC: American Geophysical Union. https://doi.org/10.1029/SP016p0087

Ueda, A., & Sakai, H. (1984). Sulfur isotope study of Quaternary volcanic rocks from the Japanese Island Arc. *Geochimica et Cosmochimica Acta*, *48*(9), 1837–1848. https://doi.org/10.1016/0016-7037(84)90037-1

Wagner, T., & Boyce, A. J. (2006). Pyrite metamorphism in the Devonian Hunsbrück Slate of Germany: Insights from laser microprobe sulfur isotope analysis and thermodynamic modeling. *American Journal of Science*, *306*(7), 525–552. https://doi.org/10.2475/07.2006.02

Wagner, T., Boyce, A. J., Jonsson, E., & Fallick, A. E. (2004). Laser microprobe sulphur isotope analysis of arsenopyrite: Experimental calibration and application to the Boliden Au-Cu-As massive sulphide deposit. *Ore Geology Reviews*, *25*(3-4), 311–325. https://doi.org/10.1016/j.oregeorev.2004.05.002

Watson, E. B., Cherniak, D. J., & Frank, E. A. (2009). Retention of biosignatures and mass-independent fractionations in pyrite: Self-diffusion of sulfur. *Geochimica et Cosmochimica Acta*, *73*(16), 4792–4802. https://doi.org/10.1016/j.gca.2009.05.060

Whitney, D. L., & Evans, B. W. (2010). Abbreviations for names of rock-forming minerals. *American Mineralogist*, *95*(1), 185–187. https://doi.org/10.2138/am.2010.3371

Wilson, M. R., Kyser, T. K., & Fagan, R. (1996). Sulfur isotope systematics and platinum group element behavior in REE-enriched meta-somatic fluids: A study of mantle xenoliths from Dish Hill, California, USA. *Geochimica et Cosmochimica Acta*, *60*(11), 1933–1942. https://doi.org/10.1016/0016-7037(96)00069-5

Woodhead, J. D., Harmons, R. S., & Fraser, D. G. (1987). O, S, Sr, and Pb isotopic variations in volcanic rocks from the Northern Mariana Islands—Implications for crustal recycling in intraoceanic arcs. *Earth and Planetary Science Letters*, *83*(1-4), 39–52. https://doi.org/10.1016/0012-821X(87)90049-5

Zajacz, Z., Seo, J. H., Candela, P. A., Piccoli, P. M., & Tossell, J. A. (2011). The solubility of copper in high-temperature magmatic vapors: A quest for the significance of various chloride and sulfide complexes. *Geochimica et Cosmochimica Acta*, *75*(10), 2811–2827. https://doi.org/10.1016/j.gca.2011.02.029

References From the Supporting Information

Altherr, R., Schliestedt, M., Okrusch, M., Seidel, E., Kreuzer, H., Harre, W., et al. (1979). Geochronology of high-pressure rocks from Sifnos (Cyclades, Greece). *Contributions to Mineralogy and Petrology*, *70*(3), 245–255. https://doi.org/10.1007/BF00375354

Anczkiewicz, B., Platt, J. P., Thirlwall, M. F., & Wakabayashi, J. (2004). Franciscan subduction off to a slow start: Evidence from high-precision Lu-Hf garnet ages on high grade-blocks. *Earth and Planetary Science Letters*, *225*(1-2), 147–161. https://doi.org/10.1016/j.epsl.2004.06.003

Baldwin, S. L. (1996). Contrasting P-T-t histories for blueschists from the western Bajan terrane and the Aegean: Effects of synsubduction exhumation and backarc extension. In G. E. Bebout, D. W. Scholl, S. H. Kirby, & J. P. Platt (Eds.), *Subduction: Top to bottom, Geophysical Monograph*, (Vol. 96, pp. 135–141). Washington DC: American Geophysical Union.

Ballévre, M., Catalán, J. R. M., López-Carmona, A., Pitra, P., Abati, J., Fernández, R. D., et al. (2014). Correlation of the nappe stack in the Ibero-Armorican arc across the Bay of Biscay: A joint French-Spanish project. *Geological Society of London, Special Publication*, *405*(1), 77–113. https://doi.org/10.1144/SP405.13

Barron, B. J., Scheibner, E., & Slansky, E. (1976). A dismembered ophiolite suite at Port Macquarie, New South Wales. *Records. Geological Survey of New South Wales*, *18*, 69–102.

Beard, B. L., Medaris, L. G., Johnson, C. M., Jelinek, E., Tonika, J., & Riciputi, L. R. (1995). Geochronology and geochemistry of eclogites from the Mariánské Lázně Complex, Czech Republic: Implications for Variscan orogenesis. *Geologische Rundschau*, *84*(3), 552–567. https://doi.org/10.1007/s005310050024

Bowes, D. R., & Aftalion, M. (1991). U-Pb zircon isotope evidence of Early Ordovician and Late Proterozoic units in the Mariánské Lázně Complex, Central European Hercynides. *Neues Jahrbuch für Mineralogie Monatshefte*, *1991*, 315–326.

Bowes, D.R., van Breemen, O., Hopgood, A.M., & Jelínek, E. (2002). 40Ar/39Ar isotopic evidence for mid-Devonian post-metamorphic pegmatite emplacement in the Mariánské Lázně Complex, Bohemian Massif, Central European Hercynides. *Neues Jahrbuch für Mineralogie Monatshefte*, *2002*(10), 445-457. https://doi.org/10.1127/0028-3649/2002/2002-0445.

Brandelik, A., & Massonne, H. J. (2004). PTGIBBS-an Excell^{TM} Visual Basic program for computing and visualizing thermodynamic functions and equilibria of rock-forming minerals. *Computers and Geosciences*, *30*(9-10), 909–923. https://doi.org/10.1016/j.cageo.2004.06.001

Bröcker, M., Bieling, D., Hacker, B., & Gans, P. (2004). High-Si phengite records the time of greenschist facies overprinting: Implications for models suggesting mega-detachments in the Aegean Sea. *Journal of Metamorphic Geology*, *22*(5), 427–442. https://doi.org/10.1111/j.1525-1314.2004.00524.x

Bröcker, M., & Franz, L. (2006). Dating metamorphism and tectonic juxtaposition on Andros Island (Cyclades, Greece): Results of a Rb-Sr Study. *Geological Magazine*, *143*(5), 609–620. https://doi.org/10.1017/S001675680600241X

Bröcker, M., & Keasling, A. (2006). Ionprobe U-Pb Zircon ages from the high-pressure/low-temperature mélange of Syros, Greece: Age diversity and the importance of pre-Eocene subduction. *Journal of Metamorphic Geology*, *24*(7), 615–631. https://doi.org/10.1111/j.1525-1314.2006.00658.x

Bröcker, M., Klemd, R., Cosca, M., Brock, W., Larionov, A. N., & Rodionov, N. (2009). The timing of eclogite facies metamorphism and migmatization in the Orlica-Snieznik complex, Bohemian Massif: Constraints from a multimethod geochronological study. *Journal of Metamorphic Geology*, *27*(5), 385–403. https://doi.org/10.1111/j.1525-1314.2009.00823.x

Bröcker, M., Kreuzer, H., Matthews, A., & Okrusch, M. (1993). ^{40}Ar/^{39}Ar and oxygen isotope studies of polymetamorphism from Tinos Island, Cycladic blueschist belt, Greece. *Journal of Metamorphic Geology*, *11*(2), 223–240. https://doi.org/10.1111/j.1525-1314.1993.tb00144.x

Bruckner, H. K., Medaris, L. G., & Bakun-Czubarow, N. (1991). Nd-Sm age and isotope patterns from Variscan eclogites of the eastern Bohemian Massif. *Neues Jahrbuch für Mineralogie (Abhandlungen)*, *163*, 169–196.

Buckman, S., Nutman, A. P., Aitchison, J. C., Parker, J., Bembrick, S., Line, T., et al. (2015). The Watonga Formation and Tacking Point Gabbro, Port Macquarie, Australia: Insights into crustal growth mechanisms on the eastern margin of Gondwana. *Gondwana Research*, *28*(1), 133–151. https://doi.org/10.1016/j.gr.2014.02.013

Cháb, J. (1973). Fosilní oceánická kůra a svrchní plášť na dnešním povrchu souší. *Věstník Ústředního ústavu geologického*, *48*, 303–310.

Crowely, Q. G., Floyd, P. A., Stedra, V., Winchester, J. A., Kachlik, V., & Holland, J. G. (2002). The Mariánské Lázně Complex, NW Bohemian Massif: Development and destruction of an early Palaeozoic seaway. *Geological Society of London, Special Publication*, *201*(1), 177–195. https://doi.org/10.1144/GSL.SP.2002.201.01.09

Dachs, E. (1986). High-pressure mineral assemblages and their breakdown products in metasediments south of the Grossvenediger, Tauern Window, Austria. *Schweizerische Mineralogische und Petrographische Mitteilungen*, *66*, 145–161.

Dachs, E., & Proyer, A. (2002). Constraints on the duration of high-pressure metamorphism in the Tauern Window from diffusion modeling of discontinuous growth zones in eclogite garnet. *Journal of Metamorphic Geology*, *20*(8), 769–780. https://doi.org/10.1046/j.1525-1314.2002.00404.x

Dallmeyer, R. D., & Urban, M. (1994). Variscan vs. Cadomian tectonothermal evolution within the Teplá-Barrandian zone, Bohemian Massif, Czech Republic: ^{40}Ar/^{39}Ar mineral and whole-rock slate/phyllite ages. *Journal of the Czech Geological Society*, *39*, 21–22.

Dixon, J. E. (1976). Glaucophane schists of Syros, Greece. *Bulletin de la Société Géologique de France*, *7*, 280.

Draper, G., & Nagle, F. (1991). Geology, structure, and tectonic development of the Rio San Juan Complex, northern Dominican Republic. In P. Mann, G. Draper, & J. F. Lewis (Eds.), *Geologic and tectonic development of the North American-Caribbean plate boundary in Hispaniola*, *Geological Society of America Special Paper*, (Vol. 262, pp. 77–95). Boulder, CO: Geological Society of America.

Dumitru, T. A., Ernst, W. G., Hourigan, J. K., & McLaughlin, R. J. (2015). Detrital zircon U-Pb reconnaissance of the Franciscan subduction complex in northwestern California. *International Geology Review*, *57*(5-8), 767–800. https://doi.org/10.1080/00206814.2015.1008060

Dumitru, T. A., Wakabayashi, J., Wright, J. E., & Wooden, J. L. (2010). Early Cretaceous transition from nonaccretionary behavior to strongly accretionary behavior within the Franciscan subduction complex. *Tectonics*, *29*, TC5001. https://doi.org/10.1029/2009TC002542

Escuder-Viruete, J., Friedman, R., Castillo-Carrión, M., Cabites, J., & Pérez-Estaún, A. (2011). Origin and significance of the ophiolitic high-P mélanges in the northern Caribbean convergent margin: Insights from the geochemistry and large-scale structure of the Rio San Juan metamorphic complex. *Lithos*, *127*(3-4), 483–504. https://doi.org/10.1016/j.lithos.2011.09.015

Escuder-Viruete, J., & Pérez-Estaún, A. (2013). Contrasting exhumation P-T paths followed by high-P rocks in the northern Caribbean subduction-accretionary complex: Insights from the structural geology, microtextures, and equilibrium assemblage diagrams. *Lithos*, *160-161*, 117–144. https://doi.org/10.1016/j.lithos.2012.11.028

Escuder-Viruete, J., Valderde-Vaquero, P., Rojas-Agramonte, Y., Gabites, J., Castillo-Carrión, M., & Pérez-Estaún, A. (2013). Timing and deformational events in the Rio San Juan complex: Implications for the tectonic controls on the exhumation of high-P rocks in the northern Caribbean subduction-accretionary prism. *Lithos*, *177*, 416–435. https://doi.org/10.1016/j.lithos.2013.07.006

Escuder-Viruete, J., Valverde-Vaquero, P., Rojas-Agramonte, Y., Gabites, J., & Pérez-Estaún, A. (2013). From intra-oceanic subduction to arc accretion and arc-continent collision: Insights from the structural evolution of the Rio San Juan metamorphic complex, northern Hispaniola. *Journal of Structural Geology*, *46*, 34–56. https://doi.org/10.1016/j.jsg.2012.10.008

Escunder-Viruete, J. (2009). *Mapa Geológico de la República Dominicana E. 1:50.000, Rio San Juan* (Map No. 6173-I). Santo Domingo: Dirección General de Minería.

Faryad, S. W. (2012). High-pressure polymetamorphic garnet growth in eclogites from the Mariánské Lázně Complex (Bohemian Massif). *European Journal of Mineralogy*, *24*(3), 483–497. https://doi.org/10.1127/0935-1221/2012/0024-2184

Faryad, S. W., Jedlicka, R., & Collett, S. (2013). Eclogite facies rocks of the Monotonous unit, clue to Variscan suture in the Moldanubian Zone (Bohemian Massif). *Lithos*, *179*, 353–363. https://doi.org/10.1016/j.lithos.2013.07.015

Frank, W., Höck, V., & Miller, C. (1987). Metamorphic and tectonic history of the central Tauern Window. In H. W. Flügel, & P. Fauple (Eds.), *Geodynamics of the Eastern Alps*, (pp. 34–54). Vienna: Deuticke.

Glen, R. A. (2005). The Tasmanides of eastern Australia. *Geological Society of London, Special Publication*, *246*(1), 23–96. https://doi.org/10.1144/GSL.SP.2005.246.01.02

Godard, G. (1988). Petrology of some eclogites in the Hercynides: The eclogites from the southern Amorican Massif. In D. C. Smith (Ed.), *Eclogites and eclogite-facies rocks, Developments in Petrology*, (Vol. 12, pp. 451–519). Amsterdam: Elsevier.

Godard, G. (2001). The Les Essarts eclogite-bearing metamorphic complex (Vendee, southern Amorican Massif, France): Pre-Variscan terrains in the Hercynian belt? *Géologie de la France*, *1-2*, 29–51.

Godard, G. (2009). Two orogenic cycles recorded in eclogite-facies gneiss from the southern Armorican Massif (France). *European Journal of Mineralogy*, *21*, 1173–1190.

Holland, T. J. B. (1970). High water activities in the generation of high pressure kyanite eclogites in the Tauern Window, Austria. *Journal of Geology*, *87*, 1–27.

Hoschek, G. (2001). Thermobarometry of metasediments and metabasites from the Eclogite Zone of the Hohe Tauern, Eastern Alps, Austria. *Lithos*, *59*(3), 127–150. https://doi.org/10.1016/S0024-4937(01)00063-9

Inger, S., & Cliff, R. A. (1994). Timing of metamorphism in the Tauern Window, Eastern Alps: Rb-Sr ages and fabric formation. *Journal of Metamorphic Geology*, *12*(5), 695–707. https://doi.org/10.1111/j.1525-1314.1994.tb00052.x

Jelínek, E., Štědrá, V., & Cháb, J. (1997). The Mariánské Lázně Complex. In S. Vrana, & V. Štědrá (Eds.), *Geological model of western Bohemia related to the KTB borehole in Germany*, *Journal of Geological Sciences*, (Vol. 47, pp. 61–70). Prague: Czech Geological Survey.

Jolivet, L., & Brun, J.-P. (2010). Cenozoic geodynamics evolution of the Aegean. *International Journal of Earth Sciences*, *99*(1), 109–138. https://doi.org/10.1007/s00531-008-0366-4

Kastl, E., & Tonika, J. (1984). The Mariánské Lázně metaophiolitic complex (west Bohemia). *Krystalinikum*, *17*, 59–76.

Keay, S. (1998). The geochronological evolution of the Cyclades, Greece: Constraints from SHRIMP U-Pb geochronology (Doctoral dissertation). Retrieved from Open Research Library. (http://hdl.handle.net/1885/145651). Canberra: Australian National University.

Keiter, M., Ballhaus, C., & Tomaschek, F. (2011). A new geological map of the island of Syros (Aegean Sea, Greece): Implications for lithostratigraphy and structural history of the Cycladic Blueschist Unit. *Geological Society of America Special Papers*, *481*, 1–43. https://doi.org/10.1130/2011.2481

Keiter, M., Piepjohn, K., Ballhaus, C., Bode, M., & Lagos, M. (2004). Structural development of high-pressure metamorphic rocks on Syros island (Cyclades, Greece). *Journal of Structural Geology*, *26*(8), 1433–1445. https://doi.org/10.1016/j.jsg.2003.11.027

Kemp, A. I. S., Hawkesworth, C. J., Collins, W. J., Gray, P. L., Blevin, P. L., & EIMF (2009). Isotopic evidence for rapid continental growth in an extensional accretionary orogen: The Tasmanides, eastern Australia. *Earth and Planetary Science Letters*, *284*(3-4), 455–466. https://doi.org/10.1016/j.epsl.2009.05.011

Košler, J., Konopásek, J., Sláma, J., & Vrána, S. (2014). U-Pb zircon provenance of Moldanubian metasediments in the Bohemian Massif. *Journal of Geological Sciences*, *171*(1), 83–95. https://doi.org/10.1144/jgs2013-059

Krebs, M., Maresch, W. V., Schertle, H.-P., Baumann, A., Draper, G., Idlemann, B., et al. (2008). The dynamics of intra-oceanic subduction zones: a direct comparison between fossil petrological evidence (Rio San Juan Complex, Dominican Republic) and numerical simulation. *Lithos*, *103*(1-2), 106–137. https://doi.org/10.1016/j.lithos.2007.09.003

Krebs, M., Schertle, H.-P., Maresch, W. V., & Draper, G. (2011). Mass flow in serpentinite-hosted subduction channels: P-T-t path patterns of metamorphic blocks in the Rio San Juan mélange (Dominican Republic). *Journal of Asian Earth Sciences*, *42*(4), 569–595. https://doi.org/10.1016/j.jseaes.2011.01.011

Krogh, E. J., Oh, C. W., & Liou, J. G. (1994). Polyphase and anticlockwise P-T evolution for Franciscan eclogites and blueschists from Jenner, California, USA. *Journal of Metamorphic Geology*, *12*(2), 121–134. https://doi.org/10.1111/j.1525-1314.1994.tb00008.x

Krogh Ravna, E. J., & Terry, M. P. (2004). Geothermobarometry of UHP and HP eclogites and schists - an evaluation of equilibria among garnet-clinopyroxene-kyranite-phengite-coesite/quartz. *Journal of Metamorphic Geology*, *22*(6), 579–592. https://doi.org/10.1111/j.1525-1314.2004.00534.x

Kurz, W., Handler, R., & Bertoldi, C. (2008). Tracing the exhumation of the Eclogite Zone (Tauern Window, Eastern Alps) by ^{40}Ar/^{39}Ar dating of white mica in eclogites. *Swiss Journal of Geosciences*, *101*, S191–S206.

Kurz, W., Neubauer, F., & Dachs, E. (1998). Eclogite meso- and microfabrics: implications for the burial and exhumation history of eclogites in the Tauern Window (Eastern Alps) from P-T-d paths. *Tectonophysics*, *285*(1-2), 183–209. https://doi.org/10.1016/S0040-1951(97)00188-1

Kurz, W., Neubauer, F., Genser, J., & Dachs, E. (1998). Alpine geodynamic evolution of passive and active continental margine sequences in the Tauern Window (eastern Alps, Austria, Italy): A review. *Geologische Rundschau*, *87*(2), 225–242. https://doi.org/10.1007/s005310050204

Kurz, W., Neubauer, F., Genser, J., Unzog, W., & Daches, E. (2001). Tectonic evolution of Pennnic Units in the Tauern Window during the Paleogene: Constraints from structural and metamorphic geology. In W. E. Piller, & M. Rasser (Eds.), *Paleogene of the Eastern Alps, Schriftenreihe der erdwissenschaftlich Kommission*, (Vol. 14, pp. 11–56). Vienna, Austria: Österreichische Akademisch der Wissenshaften.

Lagos, M., Scherer, E. E., Tomaschek, F., Münker, C., Keiter, M., Berndt, J., & Ballhaus, C. (2007). High precision Lu-Hf geochronology of Eocene eclogite-facies rocks from Syros, Cyclades, Greece. *Chemical Geology*, *243*(1-2), 16–35. https://doi.org/10.1016/j.chemgeo.2007.04.008

Lange, U., Bröcker, L., Armstrong, R., Trapp, E., & Mezger, K. (2005). Sm-Nd and U-Pb dating of high-pressure granulites from the Złote and Rychleby Mts (Bohemian Massif, Poland and Czech Republic). *Journal of Metamorphic Geology*, *23*(3), 133–145. https://doi.org/10.1111/j.1525-1314.2005.00566.x

Laurent, V., Jolivet, L., Roche, V., Augier, R., Scaillet, S., & Cardgello, G. L. (2016). Strain localization in a fossilized subduction channel: Insights from the Cycladic Blueschist Unit (Syros, Greece). *Tectonophysics*, *672-673*, 150–169. https://doi.org/10.1016/j.tecto.2016.01.036

Lister, G. S., Banga, G., & Feenstra, A. (1984). Metamorphic core complexes of cordilleran type in the Cyclades, Aegean Sea, Greece. *Geology*, *12*(4), 221–225. https://doi.org/10.1130/0091-7613(1984)12<221:MCCOCT>2.0.CO;2

Maluski, H., Bonneau, M., & Kienast, J. R. (1987). Dating metamorphic events in the Cycladic area: 40Ar/39Ar data from metamorphic rocks on the island of Syros (Greece). *Bulletin de la Socété Géologique France*, *8*, 833–842.

Marschall, H.R. (2005). Lithium, beryllium and boron in high-pressure metamorphic rocks from Syros (Greece) (Doctoral dissertation). Heidelberg, Germany: Universität Heidelberg [doi: 10.11588/heidok.00005634].

Marschall, H. R., Altherr, R., Gméling, K., & Kasztovszky, Z. (2009). Lithium, boron and chlorine as tracers for metasomatism in high-pressure metamorphic rocks: A case study from Syros (Greece). *Mineralogy and Petrology*, *95*(3-4), 291–302. https://doi.org/10.1007/s00710-008-0032-3

Marschall, H. R., Altherr, R., Ludwig, T., Kalt, A., Gméling, K., & Kasztovszky, Z. (2006). Partitioning and budget of Li, Be and B in high-pressure metamorphic rocks. *Geochimica et Cosmochimica Acta*, *70*, 4750–4769.

Mauler, A., Godard, G., & Kunze, K. (2001). Crystallographic fabrics of omphacite, rutile, and quartz in Vendée eclogites (Armorican Massif, France): Consequences for deformation mechanisms and regimes. *Tectonophysics*, *342*(1-2), 81–112. https://doi.org/10.1016/S0040-1951(01)00157-3

McDowell, F., Lehman, D. J., Gucwa, P. R., Fritz, D., & Maxwell, J. C. (1984). Glaucophane schists and ophiolites of the northern California Coast Ranges: Isotopic ages and their tectonic implications. *Geological Society of America Bulletin*, *95*(11), 1373–1382. https://doi.org/10.1130/0016-7606(1984)95<1373:GSAOOT>2.0.CO;2

McLaughlin, R. J., Kling, S. A., Poore, R. Z., McDougall, K., & Beutner, E. C. (1982). Post-Middle Miocene accretion of Franciscan rocks, northwestern California. *Geological Society of America Bulletin*, *93*(7), 595–605. https://doi.org/10.1130/0016-7606(1982)93<595:PMAOFR>2.0.CO;2

Miller, C., Konzett, J., Tiepolo, M., Armstrong, R. A., & Thöni, M. (2007). Jadeite-gneiss from the Eclogite Zone, Tauern Window, Eastern Alps, Austria: Metamorphic, geochemical and zircon record of a sedimentary protolith. *Lithos*, *93*(1-2), 68–88. https://doi.org/10.1016/j.lithos.2006.03.045

Miller, D. P., Marschall, H. R., & Schumacher, J. C. (2008). Metasomatic formation and petrology of blueschist-facies hybrid rocks from Syros (Greece): Implications for reactions at the slab-mantle interface. *Lithos*, *107*, 53–67.

Nahodilová, R., Štípská, P., Powell, R., Košler, J., & Racek, M. (2014). High-Ti muscovite as a prograde relict in high pressure granulites with metamorphic Devonian zircon ages (Běstvina granulite body, Bohemian Massif): consequences for the relamination model of subducted crust. *Gondwana Research*, *25*(2), 630–648. https://doi.org/10.1016/j.gr.2012.08.021

Nutman, A., Buckman, S., Hidaka, H., Kamiichi, T., & Belousova, E. (2013). Middle Carboniferous-Early Triassic eclogite-blueschist blocks within a serpentinite mélange at Port Macquarie, eastern Australia: Implications for the evolution of Gondwana's eastern margin. *Gondwana Research*, *24*(3-4), 1038–1050. https://doi.org/10.1016/j.gr.2013.01.009

O'Brien, P. J., & Vrána, S. (1995). Eclogites with a short-lived granulite facies overprint in the Moldanubian Zone, Czech Republic: Petrology, geochemistry and diffusion modeling of garnet zoning. *Geologische Rundschau*, *84*(3), 473–488. https://doi.org/10.1007/s005310050019

Och, D. J., Leitch, E. C., & Caprarelli, G. (2007). Geological Units of the Port Macquarie-Tacking Point tract, north-eastern Port Macquarie Block, mid north coast region of New South Wales. *Quarterly Notes Geological Survey of New South Wales*, 126.

Och, D. J., Leitch, E. C., Caprarelli, G., & Watanabe, T. (2003). Blueschist and eclogite in tectonic mélange, Port Macquarie, New South Wales, Australia. *Mineralogical Magazine*, *67*(4), 609–624. https://doi.org/10.1180/0026461036740121

Okrusch, M., & Bröcker, M. (1990). Eclogites associated with high-grade blueschists in the Cycladic archipelago, Greece: A review. *European Journal of Mineralogy*, *2*(4), 451–478. https://doi.org/10.1127/ejm/2/4/0451

Page, F. Z., Armstrong, L. S., Essene, E. J., & Mukasa, S. B. (2007). Prograde and retrograde history of the Junction School eclogite, California, and an evaluation of garnet-phengite-clinopyroxene thermobarometry. *Contributions to Mineralogy and Petrology*, *153*(5), 533–555. https://doi.org/10.1007/s00410-006-0161-9

Peucat, J. J., Vidal, P., Godard, G., & Postaire, B. (1982). Precambrian U-Pb zircon ages in eclogites and garnet pyroxenites from South-Brittany (France): An old oceanic crust in the West European Hercynian belt? *Earth and Planetary Science Letters*, *60*(1), 70–78. https://doi.org/10.1016/0012-821X(82)90021-8

Philippon, M., Gueydan, F., Pitra, P., & Brun, J.-P. (2013). Preservation of subduction-related prograde deformation in lawsonite pseudomorph-bearing rocks. *Journal of Metamorphic Geology*, *31*(5), 571–583. https://doi.org/10.1111/jmg.12035

Phillips, G., Offler, R., Rubatto, D., & Phillips, D. (2015). High-pressure metamorphism in the southern New England Orogen: Implications for long-lived accretionary orogenesis in eastern Australia. *Tectonics*, *34*, 1979–2010. https://doi.org/10.1002/2015TC003920

Prince, C. I., Košler, J., Vance, D., & Günther, D. (2000). Comparison of laser ablation ICP-MS and isotope dilution REE analyses - implications for Sm-Nd geochronology. *Chemical Geology*, *168*(3-4), 255–274. https://doi.org/10.1016/S0009-2541(00)00203-5

Putlitz, B., Cosca, M. A., & Schumacher, J. C. (2005). Prograde mica ^{40}Ar/^{39}Ar growth ages recorded in high-pressure rocks (Syros, Cyclades, Greece). *Chemical Geology*, *214*(1-2), 79–98. https://doi.org/10.1016/j.chemgeo.2004.08.056

Raith, M., Mehrens, C., & Thöle, W. (1980). Gliederung, tektonischer Bau und metamorphe Entwicklung der penninischen Serien im südlichen Venediger-Gebiet, Osttirol. *Jahrbuch der Geologischen Bundesanstalt*, *123*, 1–37.

Ridley, J. (1984). Evidence of a temperature-dependent "blueschist" to "eclogite" transformation in high-pressure metamorphism of metabasic rocks. *Journal of Petrology*, *25*(4), 852–870. https://doi.org/10.1093/petrology/25.4.852

Ring, E., Glodny, J., Will, T., & Thomson, S. N. (2010). The Hellenic subduction system: High-pressure metamorphism, exhumation, normal faulting, and large-scale extension. *Annual Reviews in Earth and Planetary Science*, *38*(1), 45–76. https://doi.org/10.1146/annurev.earth.050708.170910

Rosenbaum, G., Avigad, D., & Sánchez-Gómez, M. (2002). Coaxial flattening at deep levels of orogenic belts: Evidence from blueschists and eclogites on Syros and Sifnos (Cyclades, Greece). *Journal of Structural Geology*, *24*(9), 1451–1462. https://doi.org/10.1016/S0191-8141(01)00143-2

Royden, L. H. (1993). Evolution of retreating subduction boundaries formed during continental collision. *Tectonics*, *12*(3), 629–638. https://doi.org/10.1029/92TC02641

Schertl, H. P., Maresch, W. V., Stanek, K. P., Hertwig, A., Krebs, M., Baese, M., & Sergeev, S. S. (2012). New occurences of jadeitite, jadeite quartzite and jadeite-lawsonite quartzite in the Dominican Republic, Hispaniola: Petrological and geochronological overview. *European Journal of Mineralogy*, *24*(2), 199–216. https://doi.org/10.1127/0935-1221/2012/0024-2201

Schmid, S., Scharf, A., Handy, M. R., & Rosenberg, C. L. (2013). The Tauern Window (Eastern Alps, Austria): a new tectonic map, with cross-sections and a tectonometamorphic synthesis. *Swiss Journal of Geosciences*, *106*(1), 1–32. https://doi.org/10.1007/s00015-013-0123-y

Schumacher, J. C., Brady, J. B., Cheney, J. T., & Tonnsen, R. R. (2008). Glaucophane-bearing marbles on Syros, Greece. *Journal of Petrology*, *49*(9), 1667–1686. https://doi.org/10.1093/petrology/egn042

Spear, F. S., & Franz, G. (1986). P-T evolution of metasediments from the Eclogite Zone, south-central Tauern Window, Austria. *Lithos*, *19*(3-4), 219–234. https://doi.org/10.1016/0024-4937(86)90024-1

Stampfli, G. M. (2000). Tethyan oceans. *Geological Society of London, Special Publication*, *173*(1), 1–23. https://doi.org/10.1144/GSL.SP.2000.173.01.01

Štědrá, V. (2001). Tectonometamorphic evolution of the Mariánské Lázně Complex, Western Bohemia, based on the study of metabasic rocks (Doctoral dissertation). Prague, Czech Republic: Charles University.

Stöckhert, B., Massonne, H.-J., & Nowlan, E. U. (1997). Low differential stress during high pressure metamorphism: The microstructural record of a metapelite from the Eclogite Zone, Tauern Window, Eastern Alps. *Lithos*, *41*(1-3), 103–118. https://doi.org/10.1016/S0024-4937(97)82007-5

Teipel, U., Finger, F., & Rohrmüller, J. (2012). Remnants of Moldanubian HP-HT granulites in the eastern part of the Bavarian Forest (southwestern Bohemian Massif): Evidence from SHRIMP zircon dating and whole rock geochemistry. *Zeitschrift der Deutschen Gesellschaft für Geowissenschaften*, *163*(2), 137–152. https://doi.org/10.1127/1860-1804/2012/0163-0137

Timmermann, H., Štědrá, V., Gerdes, A., Noble, S. R., Parrish, R. R., & Dörr, W. (2004). The problem of dating high-pressure metamorphism: AU-PB isotope and geochemical study on eclogites and related rocks of the Mariánské Lázně Complex, Czech Republic. *Journal of Petrology*, *45*(7), 1311–1338. https://doi.org/10.1093/petrology/egh020

Tomaschek, F., Kennedy, A. K., Villa, I. M., Lagos, M., & Ballhaus, C. (2003). Zircons from Syros, Cyclades, Greece-Recrystallization and mobilization of zircon during high-pressure metamorphism. *Journal of Petrology*, *44*(11), 1977–2002. https://doi.org/10.1093/petrology/egg067

Trotet, F., Jolivet, L., & Vidal, O. (2001). Tectono-metamorphic evolution of Syros and Sifnos islands (Cyclades, Greece). *Tectonophysics*, *338*(2), 179–206. https://doi.org/10.1016/S0040-1951(01)00138-X

Tsujimori, T., Matsumoto, K., Wakabayashi, J., & Liou, J. G. (2006). Franciscan eclogite revisited: Reevaluation of the P-T evolution of tectonic blocks form Tiburon Peninsula, California, USA. *Mineralogy and Petrology*, *88*(1-2), 243–267. https://doi.org/10.1007/s00710-006-0157-1

Wakabayashi, J. (2017). Structural context and variation of ocean plate stratigraphy, Franciscan Complex, California: Insight into mélange origins and subduction-accretion processes. *Progress in Earth and Planetary Science*, *4*(1), 18. https://doi.org/10.1186/s40645-017-0132-y

Wood, R. M. (1982). The Laytonville Quarry (Mendocino County California) exotic block: iron-rich blueschist-facies subduction-zone metamorphism. *Mineralogical Magazine*, *45*(337), 87–99. https://doi.org/10.1180/minmag.1982.045.337.10

Zimmermann, R., Hammerschmidt, K., & Franz, G. (1994). Eocene high pressure metamorphism in the Penninic units of the Tauern Window (Eastern Alps): Evidence from ^{40}Ar-^{39}Ar dating and petrological investigations. *Contributions to Mineralogy and Petrology*, *117*(2), 175–186. https://doi.org/10.1007/BF00286841

Zulauf, G. (1997). Constriction due to subduction: Evidence for slab pull in the Mariánské Lázně Complex (central European Variscides). *Terra Nova*, *9*, 21.